



HAL
open science

Modular implementation framework of partitioned path-following strategies: Formulation, algorithms and application to the finite element software Cast3M

Hugo Luiz Oliveira, Giuseppe Rastiello, Alain Millard, Ibrahim Bitar, Benjamin Richard

► To cite this version:

Hugo Luiz Oliveira, Giuseppe Rastiello, Alain Millard, Ibrahim Bitar, Benjamin Richard. Modular implementation framework of partitioned path-following strategies: Formulation, algorithms and application to the finite element software Cast3M. *Advances in Engineering Software*, 2021, 161, pp.103055. <10.1016/j.advengsoft.2021.103055>. <hal-03762225>

HAL Id: hal-03762225

<https://hal.science/hal-03762225v1>

Submitted on 16 Oct 2023

HAL is a multi-disciplinary open access archive for the deposit and dissemination of scientific research documents, whether they are published or not. The documents may come from teaching and research institutions in France or abroad, or from public or private research centers.

L'archive ouverte pluridisciplinaire HAL, est destinée au dépôt et à la diffusion de documents scientifiques de niveau recherche, publiés ou non, émanant des établissements d'enseignement et de recherche français ou étrangers, des laboratoires publics ou privés.



Distributed under a Creative Commons CC BY-NC 4.0 - Attribution - Non-commercial use - International License



HAL
open science

Modular implementation framework of partitioned path-following strategies: Formulation, algorithms and application to the finite element software Cast3M

Hugo Luiz Oliveira, Giuseppe Rastiello, Alain Millard, Ibrahim Bitar,
Benjamin Richard

► To cite this version:

Hugo Luiz Oliveira, Giuseppe Rastiello, Alain Millard, Ibrahim Bitar, Benjamin Richard. Modular implementation framework of partitioned path-following strategies: Formulation, algorithms and application to the finite element software Cast3M. *Advances in Engineering Software*, 2021, 161, pp.103055. 10.1016/j.advengsoft.2021.103055 . hal-03762225v2

HAL Id: hal-03762225

<https://hal.science/hal-03762225v2>

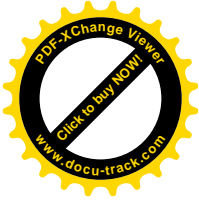
Submitted on 4 Dec 2023

HAL is a multi-disciplinary open access archive for the deposit and dissemination of scientific research documents, whether they are published or not. The documents may come from teaching and research institutions in France or abroad, or from public or private research centers.

L'archive ouverte pluridisciplinaire **HAL**, est destinée au dépôt et à la diffusion de documents scientifiques de niveau recherche, publiés ou non, émanant des établissements d'enseignement et de recherche français ou étrangers, des laboratoires publics ou privés.



Distributed under a Creative Commons Attribution - NonCommercial - NoDerivatives | 4.0
International License



Modular implementation framework of partitioned path-following strategies: formulation, algorithms and application to the finite element software Cast3M

Hugo Luiz Oliveira^a, Giuseppe Rastrello^a, Alain Millard^a, Ibrahim Bitar^b, Benjamin Richard^b

^aUniversité Paris-Saclay, CEA, Service d'études mécaniques et thermiques, 91191, Gif-sur-Yvette, France

^bInstitut de Radioprotection et de Sûreté Nucléaire (IRSN), PSN-EXP/SES/LMAPS, 92262 Fontenay-aux-Roses Cedex, France

Abstract

Damage, cracking, and strain localization mechanisms often lead to unstable structural responses characterized by snap-backs (i.e., force and displacement decrease simultaneously). Standard nonlinear Newton-based solution algorithms with displacement/force control cannot capture the equilibrium curve in its entirety. This can be overcome using path-following formulations. A general (i.e., valid for any finite element code) implementation framework can be designed and applied to the Cast3M software by collecting the essential concepts and the formalism of partitioned path-following arc-length algorithms. Thanks to these developments, Cast3M is now capable of processing path-following equations without any major modifications. Three path-following constraints were selected to demonstrate the applicability of this framework: a first one on the combination of the displacement increment at a given set of nodes, a second one on the maximum strain increment over the computational domain, and a third one on the maximum elastic predictor of the damage/plastic criterion function over the computational domain. Two- and three-dimensional strain localization simulations show that the proposed framework behaves in a stable and convergent manner, even when multiple severe snap-back instabilities are present. Users of Cast3M shall find the proposed study helpful in that it allows them to focus on developing new path-following equations for the software. Cast3M is developed by the French Alternative Energies and Atomic Energy Commission (CEA) and freely available for research purposes. The developments discussed in this paper have been made available to the user/developer community along with Cast3M 2021 (release date: June 2021).

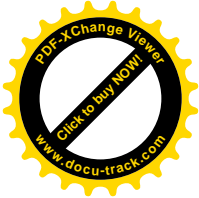
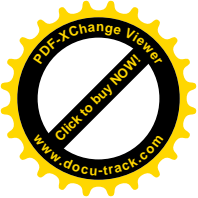
Keywords: Path-following methods, Snap-back response, Nonlinear material models, Strain localization, Cast3M software

1. Introduction

Stability is a constant worry in most activities related to the design and construction of structures. This importance comes from the fact that, without stability, one can hardly guarantee that the structures will fulfill the requirements for

*Corresponding author

Email address: giuseppe.rastrello@cea.fr (Giuseppe Rastrello)



4 which they were designed. A lack of stability can have disastrous consequences.

5 Scientific literature generally distinguishes between two sources of instabilities: geometrical instabilities, which
6 are induced by large displacements (Riks, 1972, Ramm, 1981, Crisfield, 1981); and material-induced instabilities
7 (De Borst, 1987, Verhoosel et al., 2009a, Rastiello et al., 2019). The mathematical principles leveraged in analyses of
8 the latter type of instability originate in the work of Hadamard (1903) for elastic materials, and Hill (1962), Mandel
9 (1966), Thomas (1961), Rice (1976), Needleman and Rice (1978) for elastoplastic materials. In this approach, the
10 localization phenomena are associated with a loss of ellipticity of the governing equations, which may lead to the
11 formation of shear bands depending on the ductility of the material. For quasi-brittle materials, it may also be associ-
12 ated with dissipative phenomena occurring at the material level (e.g., cracking and strain localization (Bažant, 2000)).
13 Both sources of instability may sometimes coexist (Verhoosel et al., 2009a, Bellora and Vescovini, 2016).

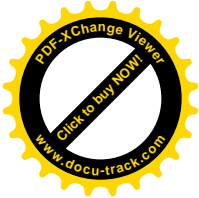
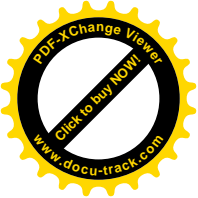
14 This work focuses on material-induced instabilities that are currently encountered in computational fracture/damage
15 mechanics. The developed framework is, however, general, and can be used to treat geometrical nonlinearities.

16 Fracture and strain localization phenomena are often responsible for unstable structural responses characterized by
17 snap-backs (De Borst, 1987), i.e., new equilibrium configurations are found, leading to a decrease in both external
18 loads and displacements. In that case, standard Newton-based procedures, which rely on force and displacement
19 control, actually fall short and show discontinuities in the force-displacement equilibrium curves. From a structural
20 mechanics viewpoint, these discontinuities represent a loss of information because they hide equilibrium states that
21 may be relevant. From a numerical modeling viewpoint, these “jumps” correspond to abrupt changes in the constitu-
22 tive model’s internal variables, with detrimental effects on the convergence of the solution algorithm.

23 The so-called “continuation” (in the mathematics community) or “path-following” (in the engineering community)
24 methods provide a solution to this issue of discontinuity. Riks (1979) first suggested that the control variable during
25 the analysis should neither be a displacement nor a force and that these should be controlled indirectly instead. In
26 order to handle non-linearity, an additional unknown and a supplementary equation, the path-following equation, are
27 required. Despite the significant benefits of Riks’ proposal, following it means that one ends up solving an augmented
28 equilibrium problem where the stiffness-like matrix that needs to be inverted is non-symmetric. To solve this issue,
29 Crisfield (1981, 1983) proposed a specific way of splitting the displacement correction, which allowed for the use
30 of classical solvers without any modifications. In that case, the displacement correction can be computed during the
31 iterative solution process in a partitioned/staggered manner.

32 The global constraint equations¹ proposed in (Riks, 1979, Crisfield, 1981, Ramm, 1981) may be well suited for
33 geometrical instabilities, but they may fail in the presence of structural instabilities induced by material non-linearities,
34 especially when localization phenomena occur (De Borst, 1987). In that case, only a limited number of DOFs is

¹Called “global” since they account for all degrees of freedom (DOFs) of the problem.



35 responsible for the unstable response observed at the structural level, and specific constraint equations have to be
36 written.

37 Since De Borst (1987)'s work, many algorithms have been proposed in the literature to overcome these limitations.
38 Among these, are worth mentioning: constraint equations on the rate of variation of selected sets of DOFs (De Borst,
39 1987, May and Duan, 1997); on strain measures (Chen and Schreyer, 1990, Geers, 1999, Pohl et al., 2014); or
40 quantities associated with the energy dissipation occurring in the system during the development of non-linearities
41 (Gutiérrez, 2004, Verhoosel et al., 2009b, Lorentz and Badel, 2004, Singh et al., 2016, Stanić and Brank, 2017,
42 Barbieri et al., 2017). Mixed path-following approaches in terms of stresses, strains, displacements, damage, and
43 other variables were also proposed (Garcea et al., 1998, Formica et al., 2002, Bilotta et al., 2012, Magisano et al.,
44 2017, 2019) to improve the convergence of standard path-following methods.

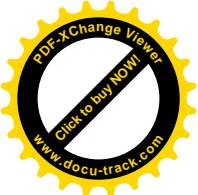
45 These techniques were successfully used in finite element simulations where the material response was modeled
46 using local and nonlocal continuum damage mechanics laws (Lorentz and Badel, 2004, Rastiello et al., 2018, Thierry
47 et al., 2020), phase-field models (Singh et al., 2016), and Thick Level-Set (TLS) damage formulations (Moreau et al.,
48 2017). Path-following methods were also used in strong discontinuity simulations of failure in solids, where cracks
49 were represented as zero-thickness interface finite elements (Alfano and Crisfield, 2003, Lorentz and Badel, 2004),
50 according to the extended (Massin et al., 2011, Wang and Waisman, 2018) or the embedded finite element method
51 (Oliver et al., 2008, Brank et al., 2016, Cazes et al., 2016, Rastiello et al., 2019).

52 This overview of the evolution of path-following methods reveals the essential aspects of the present work. Firstly,
53 although remarkable advances have been made in the last decades, the theoretical framework established in the pio-
54 neering works by Riks (1972), Crisfield (1981), and De Borst (1987) remains unchanged. Secondly, the numerical
55 procedures discussed above still haven't been made available to the Cast3M users community.²

56 These two aspects bring us to the main purpose of this study, namely proposing a general framework, applicable to
57 the Cast3M software, capable of processing instabilities generated by strain localization. The proposed framework is
58 designed in a flexible and modular way to make the study of new path-following conditions possible. In this case, the
59 proposed framework can serve as the starting point for further investigations involving path-following methodologies.

60 This paper is structured as follows. First, the boundary value problem that needs solving is presented according to
61 the formalism of path-following theories. Then, the procedure used to find the solution of the problem is abstracted
62 in order to create the proposed framework. This framework's main feature is its modularity; that is, it is designed to
63 allow Cast3M to accept different user-defined path-following conditions without modifying the framework. Once the
64 framework is introduced, three path-following equations are detailed. These will showcase how to use the proposed
65 framework. These criteria are of practical interest and encompass both dissipative and non-dissipative formulations.

²Cast3M (<http://www-cast3m.cea.fr/index.php>) is a well-established finite element software (Verpeaux et al., 1989) developed and distributed by the CEA, the French Alternative Energies and Atomic Energy Commission (<https://www.cea.fr/english>).



66 Finally, representative two and three-dimensional case studies involving one or more snap-back phases are discussed.

67 The paper ends with a summary of the findings.

68 **2. Path-following methods**

69 This section starts with the introduction of the boundary value problem that needs solving. Then, some dissipative
 70 and non-dissipative path-following constraints are introduced. The term “dissipative” refers to constraint equations
 71 which only describe dissipative solutions (i.e., the dissipation in the system stays positive). Conversely, the term
 72 “non-dissipative” refers to constraint equations in which this characteristic is not fulfilled. In other words, one can
 73 also describe artificial/elastic unloading paths. Finally, some details concerning the discrete finite element problem
 74 are given.

75 *2.1. Boundary value problem*

76 Let $\Omega \subset \mathbb{R}^n$ (with $n = 1, 2, 3$ the problem’s dimension) represent the structure of interest (fig. 1) for this study and
 77 $t \in [0, T]$ be the pseudo-time under consideration. The boundary $\partial\Omega \subset \mathbb{R}^n$ of the structure is composed of two
 78 complementary parts: $\partial\Omega_u \subset \partial\Omega$, where the external actions can be specified in terms of displacements (Dirichlet
 79 boundary conditions) and $\partial\Omega_t \subset \partial\Omega$, where the external actions are defined in terms of forces (Neumann boundary
 conditions). Moreover \mathbf{n} denotes the outward normal vector field to $\partial\Omega$.

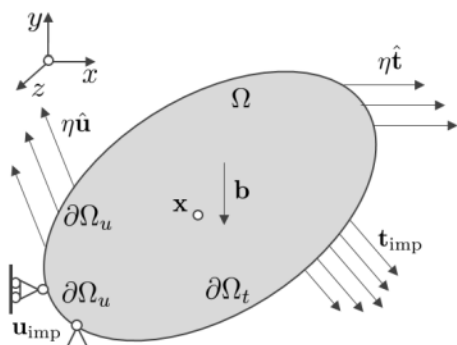
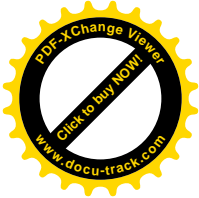
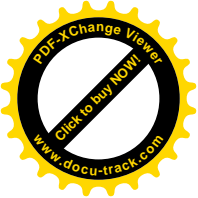


Figure 1: General domain of study.

80

81 Under the small perturbations assumption, solving the time-independent boundary value problem (BVP) consists in
 82 finding the vector-valued displacement field $\mathbf{u} = \mathbf{u}(\mathbf{x}, t)$ and the real scalar parameter η such that:



$$\nabla \cdot \boldsymbol{\sigma}(\mathbf{u}) + \mathbf{b} = 0 \quad \mathbf{x} \in \Omega \quad (1)$$

$$\boldsymbol{\sigma}(\mathbf{u}) = \mathcal{A}(\boldsymbol{\epsilon}(\mathbf{u})) \quad \mathbf{x} \in \Omega \quad (2)$$

$$\boldsymbol{\epsilon}(\mathbf{u}) = \text{Sym}(\nabla \mathbf{u}) \quad \mathbf{x} \in \Omega \quad (3)$$

$$\mathbf{u} = \mathbf{u}_{\text{imp}} + \eta \hat{\mathbf{u}} \quad \mathbf{x} \in \partial\Omega_u \quad (4)$$

$$\boldsymbol{\sigma} \cdot \mathbf{n} = \mathbf{t}_{\text{imp}} + \eta \hat{\mathbf{t}} \quad \mathbf{x} \in \partial\Omega_t \quad (5)$$

$$p(\mathbf{u}, \eta) = 0 \quad \mathbf{x} \in \Omega \quad (6)$$

83 where $\boldsymbol{\sigma}(\mathbf{u})$ stands for the Cauchy stress tensor, $\boldsymbol{\epsilon}(\mathbf{u})$ is the infinitesimal strain tensor, \mathcal{A} is the constitutive relationship
 84 between $\boldsymbol{\sigma}$ and $\boldsymbol{\epsilon}$, Sym denotes the symmetric part operator, \mathbf{u}_{imp} is the imposed displacement, $\hat{\mathbf{u}}$ is the direction of
 85 the indirectly-controlled displacement, \mathbf{t}_{imp} is the imposed traction vector, $\hat{\mathbf{t}}$ is a vector providing the direction of
 86 the indirectly-controlled tractions, “ $\nabla \cdot$ ” denotes the divergence operator and “ ∇ ” the gradient. Finally, $p(\mathbf{u}, \eta)$ is the
 87 path-following constraint equation.

88 2.2. Finite Element formulation

89 The finite element formulation of the BVP can easily be derived once the problem has been rewritten in its variational
 90 form using the Principle of Virtual Works (Hughes, 1987, Zienkiewicz et al., 2005, De Borst et al., 2012). Once the
 91 variational formulation is established, a finite element discretization Ω^h of Ω is considered. This discretization is such
 92 that inside each finite element $\Omega_e \subset \Omega^h$, the unknown field \mathbf{u} can be approximated from its nodal values (\mathbf{d}) through
 93 polynomial shape functions.

94 Using a double Lagrange multipliers formalism (Pegon and Anthoine, 1997) for imposing Dirichlet boundary condi-
 95 tions, solving the finite element problem becomes a matter of finding the nodal displacement vector \mathbf{d} , the discrete
 96 Lagrange multipliers λ_1 and λ_2 (i.e., the nodal reaction forces), and the load multiplier η such that (Richard et al.,
 97 2019):

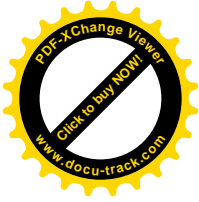
$$\begin{aligned} \mathbf{r}(\mathbf{d}, \lambda_1, \lambda_2, \eta) &= \mathbf{f}^{\text{int}}(\mathbf{d}) + \mathbf{C}^\top \lambda_1 + \mathbf{C}^\top \lambda_2 \\ &\quad - \eta \hat{\mathbf{f}}^{\text{ext}} - \mathbf{f}_{\text{imp}}^{\text{ext}} = 0 \end{aligned} \quad (7)$$

$$\mathbf{l}_1(\mathbf{d}, \lambda_1, \lambda_2, \eta) = \mathbf{C}\mathbf{d} + \lambda_1 - \lambda_2 - \eta \hat{\mathbf{d}} - \mathbf{d}_{\text{imp}} = 0 \quad (8)$$

$$\mathbf{l}_2(\mathbf{d}, \lambda_1, \lambda_2, \eta) = \mathbf{C}\mathbf{d} - \lambda_1 + \lambda_2 - \eta \hat{\mathbf{d}} - \mathbf{d}_{\text{imp}} = 0 \quad (9)$$

$$p(\mathbf{d}, \eta) = 0 \quad (10)$$

98 where $\hat{\mathbf{d}}$ is the discrete counterpart of $\hat{\mathbf{u}}$ and:



$$\mathbf{f}^{\text{int}}(\mathbf{d}) = \mathbf{A} \int_{\Omega_e} \mathbf{B}^\top \boldsymbol{\sigma}(\mathbf{d}) dv \quad (11)$$

$$\mathbf{f}_{\text{imp}}^{\text{ext}} = \mathbf{A} \int_{\Gamma_e} \mathbf{N}^\top \mathbf{s}_{\text{imp}} ds + \mathbf{A} \int_{\Omega_e} \mathbf{N}^\top \mathbf{b} dv \quad (12)$$

$$\hat{\mathbf{f}}^{\text{ext}} = \mathbf{A} \int_{\Gamma_e} \mathbf{N}^\top \hat{\mathbf{s}} dv \quad (13)$$

99 In eqs. (11) to (13) the symbol \mathbf{A} denotes the standard assembly operator over the n_{el} elements of Ω^h , \mathbf{N} is the displacement interpolation (shape function) matrix, \mathbf{B} denotes the strain-displacement matrix, “ \top ” denotes the transpose operator, and Γ_e is the element boundary. Finally, $(\mathbf{s}_{\text{imp}}, \hat{\mathbf{s}})$ are the discretized counterparts of $(\mathbf{t}_{\text{imp}}, \hat{\mathbf{t}})$.

102 According to this formulation, $\boldsymbol{\lambda} = \boldsymbol{\lambda}_1 + \boldsymbol{\lambda}_2$ corresponds to the reaction forces at the nodes where Dirichlet boundary conditions are imposed and $\boldsymbol{\lambda}_1 - \boldsymbol{\lambda}_2 = \mathbf{0}$. This formalism is the one used in Cast3M, since it prevents us from having to solve a saddle-point problem, as opposed to the use of a single set of Lagrange multipliers to enforce the Dirichlet boundary conditions (Babuška, 1973).

106 2.3. Linearized problem

107 Equations (7) to (10) are discretized in pseudo-time according to an ordered sequence of steps $[t_0, t_1, \dots, T]$, such that $t_{n+1} > t_n$ for all $n \in \mathbb{N}$, and the problem is solved in an incremental manner. Given the solution $\mathbf{x}_n = \{\mathbf{d}_n, \boldsymbol{\lambda}_{1,n}, \boldsymbol{\lambda}_{2,n}, \eta_n\}^\top$ at time t_n , one searches for $\Delta \mathbf{x} = \{\Delta \mathbf{d}, \Delta \boldsymbol{\lambda}_1, \Delta \boldsymbol{\lambda}_2, \Delta \eta\}^\top$, the solution variation in the interval $[t_n, t_{n+1}]$, such that $\mathbf{x}_{n+1} = \mathbf{x}_n + \Delta \mathbf{x}$ at time t_{n+1} .

111 Since nonlinear constitutive laws are commonly used in solid mechanics computations, the incremental problem is solved by means of an iterative procedure. Accordingly, the total solution increment at global iteration $k+1$ is written as $\Delta \mathbf{x}^{k+1} = \Delta \mathbf{x}^k + \delta \mathbf{x}^{k+1}$, where $\delta \mathbf{x}^{k+1} = \{\delta \mathbf{d}^{k+1}, \delta \boldsymbol{\lambda}_1^{k+1}, \delta \boldsymbol{\lambda}_2^{k+1}, \delta \eta^{k+1}\}^\top$ denotes the correction of the solution between iterations k and $k+1$.

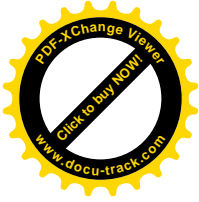
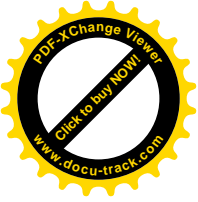
115 The subscript $n+1$ has been omitted in the previous equations for the sake of keeping them short. The same nomenclature will be used in the rest of this article. As a result, any quantity without a subscript shall actually refer to the pseudo-time step t_{n+1} .

118 2.3.1. Global equilibrium equations

119 The incremental equilibrium equations that have to be solved at each iteration arise from the linearization of eqs. (7) to (9) based on the solution at iteration k .

121 At iteration $k+1$ of the nonlinear solution process, the iterated solution is thus computed from:

$$\tilde{\mathbf{K}}^k \delta \mathbf{a}^{k+1} = -\tilde{\mathbf{r}}^k + \delta \eta^{k+1} \tilde{\mathbf{f}} \quad (14)$$



122 where:

$$\tilde{\mathbf{K}}^k = \begin{bmatrix} \mathbf{K}^k & \mathbf{C}^\top & \mathbf{C}^\top \\ \mathbf{C} & \mathbf{I} & -\mathbf{I} \\ \mathbf{C} & -\mathbf{I} & \mathbf{I} \end{bmatrix} \quad (15)$$

$$\delta \mathbf{a}^{k+1} = \{\delta \mathbf{d}^{k+1}, \delta \boldsymbol{\lambda}_1^{k+1}, \delta \boldsymbol{\lambda}_2^{k+1}\}^\top \quad (16)$$

$$\tilde{\mathbf{r}}^k = \{\mathbf{r}^k, \mathbf{l}_1^k, \mathbf{l}_2^k\}^\top \quad (17)$$

$$\tilde{\mathbf{f}} = \{\hat{\mathbf{f}}^{\text{ext}}, \hat{\mathbf{d}}, \hat{\mathbf{d}}\}^\top \quad (18)$$

123 with $\mathbf{r}^k = \mathbf{r}(\hat{\mathbf{d}}^k, \boldsymbol{\lambda}_1^k, \boldsymbol{\lambda}_2^k, \eta^k)$ and $\mathbf{l}_\bullet^k = \mathbf{l}_\bullet(\hat{\mathbf{d}}^k, \boldsymbol{\lambda}_1^k, \boldsymbol{\lambda}_2^k, \eta^k)$ (with $\bullet = 1, 2$).

124 The formalism introduced by Crisfield (1983) allows us to write the unknown vector $\delta \mathbf{a}^{k+1}$ as the sum of two inde-
125 pendent contributions:

$$\delta \mathbf{a}^{k+1} = \delta \mathbf{a}_I^{k+1} + \delta \eta^{k+1} \delta \mathbf{a}_{II}^{k+1} \quad (19)$$

126 where $\delta \mathbf{a}_I^{k+1}$ and $\delta \mathbf{a}_{II}^{k+1}$ can be calculated by simply knowing the solution at the k -th iteration:

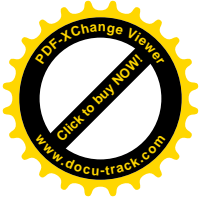
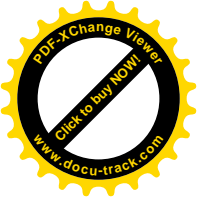
$$\delta \mathbf{a}_I^{k+1} = -(\tilde{\mathbf{K}}^k)^{-1} \tilde{\mathbf{r}}^k \quad \delta \mathbf{a}_{II}^{k+1} = (\tilde{\mathbf{K}}^k)^{-1} \tilde{\mathbf{f}} \quad (20)$$

127 2.3.2. Path-following constraint equations

128 $\delta \eta^{k+1}$ can be computed in several ways depending on the nature of the path-following equation. In particular:

- 129 (i) When function p is linear with respect to \mathbf{d} , one can obtain $\delta \eta^{k+1}$ directly.
- 130 (ii) Conversely, when p is nonlinear, it has to be linearized in order to find $\delta \eta^{k+1}$. However, such linearization
131 is not always possible, e.g., when the constraint equation is expressed by maximizing some quantity over the
132 computational domain. In that case, two options are available:
- 133 – When function p is differentiable with respect to \mathbf{d} and η . Differentiability can be guaranteed, for instance,
134 when path-following constraints are expressed in terms of sets of global DOFs fixed *a priori* (De Borst,
135 1987) or in terms of the dissipation over the whole structure (Gutiérrez, 2004, May et al., 2016, Verhoosel
136 et al., 2009a). In such a case, the linearization based on the solution at the k -th iteration gives:

$$p^k + (\mathbf{h}^k)^\top \delta \mathbf{d}^{k+1} + w^k \delta \eta^{k+1} = 0 \quad (21)$$



137

where:

$$p^k = p(\mathbf{d}^k, \eta^k) \quad (22)$$

$$\mathbf{h}^k = (\partial p / \partial \mathbf{d})^k \quad (23)$$

$$w^k = (\partial p / \partial \eta)^k \quad (24)$$

138

Finally, substituting eq. (19) into eq. (21) and solving for $\delta\eta^{k+1}$ gives:

$$\delta\eta^{k+1} = -\frac{p^k + (\mathbf{h}^k)^\top \delta\mathbf{d}_I^{k+1}}{w^k + (\mathbf{h}^k)^\top \delta\mathbf{d}_{II}^{k+1}} \quad (25)$$

139

- When general and robust constraint equations try to establish a load multiplier variation such that the field of interest $g = g(\mathbf{d}, \eta)$ (e.g., strain field variation, local energy dissipation variation, elastic predictor of the damage/plasticity criterion) over Ω^h reaches a maximum value for a user-defined step length ($\Delta\tau$).

140

141

142

This kind of constraint equations takes the following form:

$$p^{k+1} = \max_{\alpha \in \Omega^h} (g_\alpha^{k+1}) - \Delta\tau = 0 \quad (26)$$

143

where α denotes a portion (or a numerical entity) of the discretized domain (e.g., a node, an integration point). In the rest of this article, $(\bullet)_\alpha$ indicates that the quantity (\bullet) is computed at the position of the entity α .

144

145

146

The main drawback of this approach is that the maximum operator function renders (26) non-differentiable.

147

As a consequence, a direct estimation of $\delta\eta^{k+1}$ is not possible even though g_α^{k+1} is linear, or can be linearized, with respect to $\delta\eta^{k+1}$.

148

149

Nevertheless, the computation can be performed through an iterative procedure, e.g., with a nested interval algorithm (Lorentz and Badel, 2004).

150

151 2.4. Staggered solution

152

Thanks to the formalism introduced in Crisfield (1983), it is possible to solve the augmented global equilibrium problem (eqs. (7) to (10)) in a sequential manner (Algorithm 1).

153

154

Indeed, since the linearization of the equation (14) that expresses the structural equilibrium does not take into account the path-following constraint in (10), the strategy for finding a solution to the equilibrium problem preserves the essential characteristics of Newton's method, which is used in commercial FEM softwares.

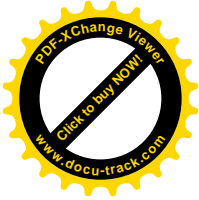
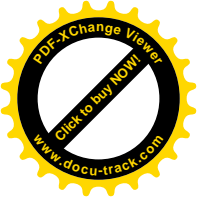
155

156

157

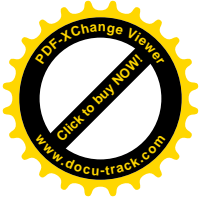
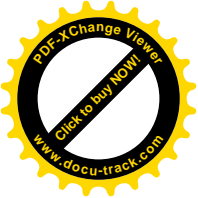
Therefore, one can implement path-following solvers in any FE analysis software provided that one can modify the main FEM matrices directly.

158



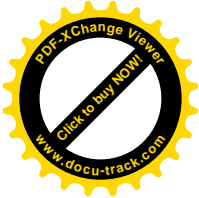
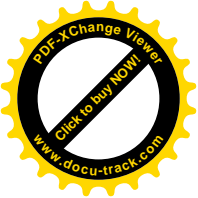
Algorithm 1: General finite element implementation of path-following solvers using the displacement breakdown method of Crisfield (1983).

```
1: conv  $\leftarrow$  0,  $k \leftarrow$  0
2:  $\mathbf{a}^k \leftarrow \mathbf{a}_n$ ,  $\eta^k \leftarrow \eta_n$ 
3:  $\Delta \mathbf{a}^k = 0$ ,  $\Delta \eta^k = 0$ 
4:  $\tilde{\mathbf{r}}^k = \tilde{\mathbf{r}}^k(\mathbf{d}^k, \lambda_1^k, \lambda_2^k, \eta^k; \mathbf{f}_{\text{imp}}^{\text{ext}}, \mathbf{d}_{\text{imp}})$ 
5: while conv = 0 do
6:   Compute  $\mathbf{K}^k$ 
7:   Build  $\tilde{\mathbf{K}}^k$ 
8:   Solve  $\tilde{\mathbf{K}}^k \delta \mathbf{a}_I^{k+1} = -\tilde{\mathbf{r}}^k$  for  $\delta \mathbf{a}_I^{k+1}$ 
9:   Solve  $\tilde{\mathbf{K}}^k \delta \mathbf{a}_{II}^{k+1} = \tilde{\mathbf{f}}$  for  $\delta \mathbf{a}_{II}^{k+1}$ 
10:  Solve the constraint equation to compute  $\delta \eta^{k+1}$ 
11:  Compute  $\eta^{k+1} \leftarrow \eta^k + \delta \eta^{k+1}$ 
12:  Compute  $\mathbf{a}^{k+1} \leftarrow \mathbf{a}^k + \delta \mathbf{a}_I^{k+1} + \delta \eta^{k+1} \delta \mathbf{a}_{II}^{k+1}$ 
13:  Compute  $\tilde{\mathbf{r}}^{k+1}$ 
14:  if Convergence is met then
15:    conv = 1
16:    Solution at time  $t_{n+1}$ :  $\eta \leftarrow \eta^{k+1}$ 
17:    Solution at time  $t_{n+1}$ :  $\mathbf{a} \leftarrow \mathbf{a}^{k+1}$ 
18:  else
19:     $k \leftarrow k + 1$ 
20:  end if
```



159 *2.5. Additional remarks*

160 If the constraint equation is linear or linearizable with respect to the unknown displacements and the load multiplier,
161 solving the problem with the Crisfield formalism (i.e., partitioned approach) is entirely equivalent to using Riks' direct
162 approach. Indeed, the solution of a non-symmetric system of equations in the Riks' approach can be circumvented
163 with the well-known Sherman-Morrison formula (May et al., 2016, Verhoosel et al., 2009a). The main advantage
164 of the partitioned approach is that differentiability of the constraint equation is not required, which increases the
165 flexibility of the developed numerical framework.



166 3. Cast3M implementation

167 This section starts with a brief presentation of the main modifications implemented in the standard nonlinear solver of
168 the code. The focus will then shift to the procedure for solving the path-following constraint equations. In particular,
169 details will be given regarding the default constraint equation and the possibility of specifying user-defined constraint
170 equations by “overloading” the standard procedure.

171 All implementations discussed in this study are carried out using the Gibiane scripting language (Ebersolt et al.,
172 1987), an object-oriented language developed, maintained, and distributed by the CEA. This language is used in
173 Cast3M (Verpeaux et al., 1989). Notice, however, that the modular implementation framework proposed herein and
174 the considered constraint equations (formulation, solving techniques) are entirely general and can be adapted to any
175 finite element software.

176 3.1. Cast3M procedures

177 The main modifications implemented in the Cast3M code concern three existing procedures (PAS_DEFA, PAS_INIT,
178 and UNPAS) of the main nonlinear incremental Cast3M solver (PASAPAS). These procedures are modified (see
179 fig. 2 for more details) in order to create and handle all the data structures for the path-following methods; to compute
180 the solution variations $\delta \mathbf{a}_I^{k+1}$ and $\delta \mathbf{a}_{II}^{k+1}$; and to build the total correction $\delta \mathbf{a}^{k+1}$ once the load multiplier variation
181 $\delta \eta^{k+1}$ has been determined. Moreover, an additional procedure called PILOINDI is added to handle the constraint
182 equation’s solution (i.e., to compute $\delta \eta^{k+1}$ depending on the selected path-following equation) once $\delta \mathbf{a}_I^{k+1}$ and $\delta \mathbf{a}_{II}^{k+1}$
183 have been determined.

184 3.2. The PILOINDI procedure and default constraint equation

185 The path-following equation implemented as the default option in the PILOINDI procedure is based on the maximiza-
186 tion of a scalar measure of the strain field variation (Control by Maximum Strain Increment, CMSI) through Ω^h or a
187 part of it, $\Omega_{\text{red}}^h \subset \Omega^h$.

188 The constraint equation reads similarly as in eq. (26), with function g_α^{k+1} defined as:

$$g_\alpha^{k+1} = \mathbf{q}_\alpha^\top \Delta \boldsymbol{\epsilon}_\alpha^{k+1} \quad (27)$$

189 with \mathbf{q}_α being the direction of the strain vector at the position of the integration point α at the previous time step:

$$\mathbf{q}_\alpha = \frac{\mathbf{B}_\alpha \mathbf{d}_n}{\|\mathbf{B}_\alpha \mathbf{d}_n\|} \quad (28)$$

190 Given the additive decomposition in eq. (19), $\Delta \boldsymbol{\epsilon}_\alpha^{k+1}$ depends linearly on $\delta \eta^{k+1}$ according to:

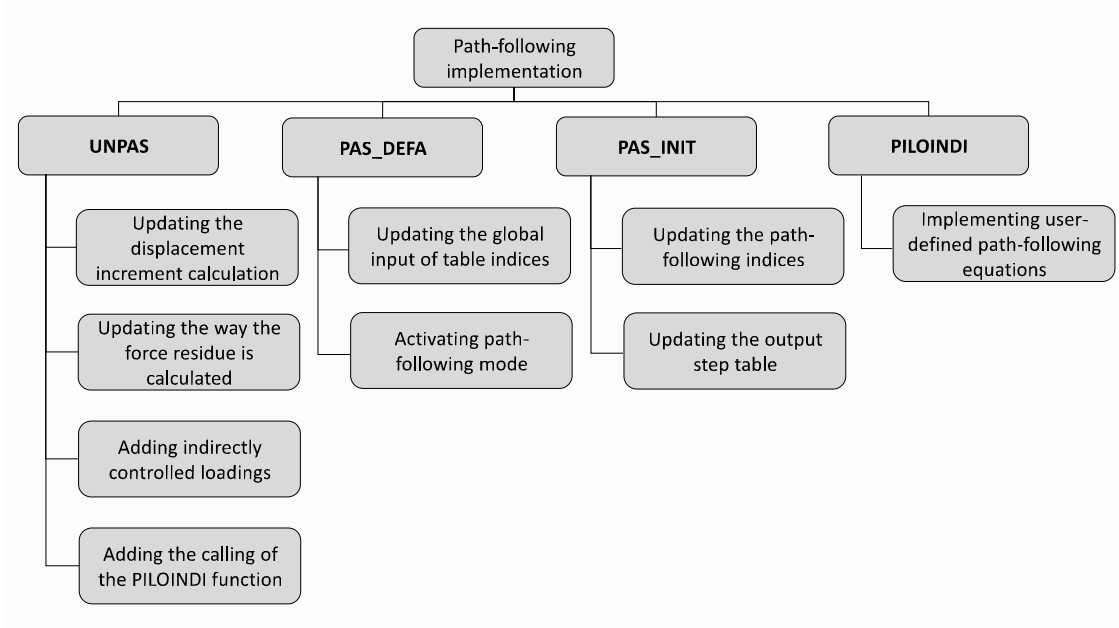


Figure 2: Schematic description of the main modifications implemented in Cast3M's nonlinear incremental solver.

$$\Delta \epsilon_{\alpha}^{k+1} = \mathbf{q}_{\alpha}^{\top} \mathbf{B}_{\alpha} (\Delta \mathbf{d}^k + \delta \mathbf{d}_I^{k+1} + \delta \eta^{k+1} \delta \mathbf{d}_{II}^{k+1}) \quad (29)$$

191 As a consequence, the constraint equation that needs to be solved can be rewritten as:

$$\max_{\alpha \in \Omega^k} (a_{0,\alpha} + a_{1,\alpha} \delta \eta^{k+1}) - \Delta \tau = 0 \quad (30)$$

192 where the coefficients $a_{0,\alpha}$ and $a_{1,\alpha}$ read:

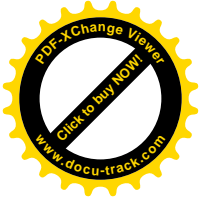
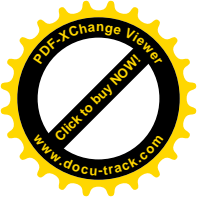
$$a_{0,\alpha} = \mathbf{q}_{\alpha}^{\top} \mathbf{B}_{\alpha} (\Delta \mathbf{d}^k + \delta \mathbf{d}_I^{k+1}) \quad (31)$$

$$a_{1,\alpha} = \mathbf{q}_{\alpha}^{\top} \mathbf{B}_{\alpha} \delta \mathbf{d}_{II}^{k+1} \quad (32)$$

193 Element-wise, function (30) is convex and linear. However, a direct determination of $\delta \eta^{k+1}$ is not possible since the
 194 maximum function is not differentiable. Instead, an iterative minimization algorithm is used.

195 Following Lorentz and Badel (2004), the method is chosen for determining the value of $\delta \eta^{k+1}$ is the nested interval
 196 method. Accordingly, the constraint equation is solved at each integration point in order to compute the load multiplier
 197 corrections $\delta \eta_{\alpha}^{k+1}$ such that:

$$a_{0,\alpha} + a_{1,\alpha} \delta \eta_{\alpha}^{k+1} - \Delta \tau = 0 \quad (33)$$



198 Then, a single $\delta\eta^{k+1}$ value is selected. More precisely, the sequence of tasks can be summarized as follows:

- 199 1. Initialize the interval $I = [-s, +s]$, where s is a very large value;
- 200 2. Loop over the integration points $\alpha \in \Omega^h$;
- 201 (a) Calculate $\delta\eta_\alpha^{k+1}$ by solving eq. (33)
- 202 (b) Update the interval I :
- 203 i. if $a_{1,\alpha} > 0 \rightarrow I = I \cap [-s, \delta\eta_\alpha^{k+1}]$
- 204 ii. if $a_{1,\alpha} < 0 \rightarrow I = I \cap [\delta\eta_\alpha^{k+1}, +s]$
- 205 3. Compute the solution:

$$\delta\eta^{k+1} \in \{\eta_{\min}, \eta_{\max}\} \quad (34)$$

206 Of the two values $\delta\eta_{\min}$ and $\delta\eta_{\max}$, the correct $\delta\eta$ value will be the one corresponding to the smallest force
 207 residue, or, alternatively, to the smallest norm $\|\delta\mathbf{d}^{k+1}\|$.

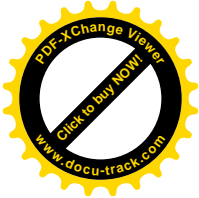
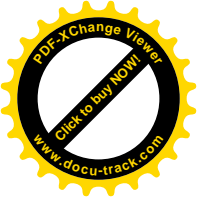
208 3.3. Building a data file

209 Using the path-following solver with the standalone implementation is easy and only requires minor modifications to
 210 existing Cast3M data files.³

211 In particular, the main steps for building the simulation file can be summarized as follows:

- 212 (i) The definition of the simulation always starts with the definition of the geometry of the problem, the definition
 213 of the material model, and the force/displacement boundary conditions. At this stage, only the known (imposed)
 214 contributions to the boundary conditions are prescribed.
- 215 (ii) Some initializations are then necessary for the path-following solver. In particular, one has to prescribe the
 216 domain's boundary over which the external load (displacement or force) is indirectly controlled. The direction
 217 of this loading is also given. In the example of listing 1 below, an indirectly-controlled horizontal displace-
 218 ment (component UX) is applied to the boundary labeled BOUNDIND. This information is stored in the object
 219 DISPIND and added to the object BCTOT together with information concerning other Dirichlet boundary con-
 220 ditions. Finally, the unity nodal field DHAT (representing $\hat{\mathbf{d}}$) for the solution process is defined.
- 221 (iii) Once DHAT has been defined, the variation of the path step length as a function of time is prescribed. The
 222 simplest solution is to consider $\Delta\tau$ a constant. However, the implementation proposed here allows it to vary as
 223 the simulation progresses, depending on the user's considerations (listing 2). For instance, one could imagine
 224 changing the path step length during the simulation in order to follow the evolution of the damage. In the simple
 225 example illustrated here, constant evolution is stored in the object called EVOLTAU. Notice that, in the code,
 226 the evolution of τ is given as an input, and that $\Delta\tau$ is computed at each time-step as $\tau - \tau_n$.

³The full syntax of the new procedure is available here: <http://www-cast3m.cea.fr/index.php?page=noticesnotice=PILOINDI>.

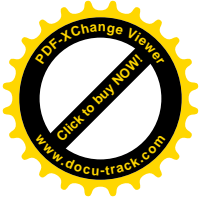
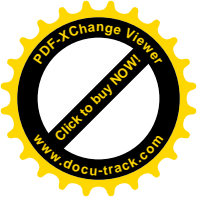


Listing 1: Syntax for using the new PILOINDI procedure (definition of the indirectly-controlled displacement).

```
*****
* Pre-processing
*
* Geometry
* Model and materials
* Boundary conditions (imposed contributions)
* ...
*****
* Initialization needed for using the
* path-following solver
*
* Direction of the indirectly-controlled
* displacement on the boundary labeled BOUNDIND
* ('UX','UY','UZ') stand for the displacements
* along the (X,Y,Z) directions.
DISPIND = 'BLOQ' 'UX' BOUNDIND;
*
* Add this indirectly-controlled boundary
* condition to other Dirichlet boundary
* conditions CLT
BCTOT = BCTOT 'ET' DISPIND;
*
* Create the unity field defining the direction
* of the indirectly-controlled displacement
* applied to LATD
DHAT = 'DEPI' CL3 1.0 ;
*****
```

227 (iv) The data structures for running the nonlinear solving process are then created (listing 3). This information is
228 stored in the object called TAB1. The user then provides, in addition to standard commands used with the
229 incremental PASAPAS solver, three additional pieces of information to: activate the path-following solver,
230 know if one indirectly controls displacements or forces, and give the evolution of τ . An optional fourth piece of
231 information can also be provided regarding the definition of the part of the mesh on which the maximum of the
232 constraint equation must be sought. If this last piece of information isn't provided, the maximization is done
233 over the whole finite element mesh.

234 (v) Finally, one can run the PASAPAS solver and proceed with the post-processing of the obtained results, as usual
235 with Cast3M.



Listing 2: Syntax for using the new **PILOINDI** procedure (evolution of the time-step length parameter).

```
*****
* Maximum number of pseudo-time steps
NS=100;

* Definition of the path step length
* Reference value for tau
TAU = 7.0E-5;

* Create a variation as a function of time for
* the path step length parameter
LIS1 = PROG 0. PAS TAU (NS * TAU) ;
EVOLTAU = EVOL MANU 't' LIS1 'tau' LIS1 ;
*****
```

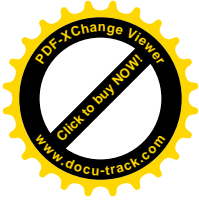
Listing 3: Syntax for using the new **PILOINDI** procedure (activation of the path-following solver).

```
*****
* Standard definition of the data structure needed
* for using the nonlinear incremental solver
* PASAPAS
  TAB1 = TABLE;
  TAB1 . mova = ...;
  ...
*****
* Lines to include for the activation of the
* path-following solver

  * activate the path-following solver
  * VRAI = TRUE, FAUX = FALSE
  TAB1 . 'PILOTAGE_INDIRECT' = VRAI ;

  * indirectly-controlled force or displacement
  * use uch for displacement and fch for force
  TAB1 . 'DEPLACEMENTS_PILOTES' = DHAT ;

  * pseudo-time evolution of the path step
  * length parameter
  TAB1 . 'PARAMETRE_DE_PILOTAGE' = EVOLTAU;
*****
* Run the simulation using the nonlinear solver
* PASAPAS with path-following methods
  PASAPAS TAB1;
*****
* Post-processing
  ...
*****
```



236 **4. User-defined constraint equations**

237 The CMSI formulation can be used without needing to perform any additional developments. However, user-defined
238 constraint equations can be added in a standalone manner by overloading the `PILOINDI` procedure in the simulation's
239 script (i.e., without touching the source code). The general syntax used to write new constraint equations is presented
240 in Listing 4.

241 Two possible user-defined constraints are implemented to showcase this feature:

- 242 (i) The first constraint equation, the so-called Control by Nodal Displacement Increment (CNDI), is fully general
243 (De Borst, 1987) and can be used with any material model. It is particularly interesting for simulating exper-
244 imental loading conditions; for instance, when a combination of displacement measures is used to drive the
245 variation of the external load (see, e.g., Rastiello et al. (2014, 2015)).
- 246 (ii) The second constraint equation is more model-dependent since it relies on Controlling the Maximum Elastic
247 Predictor (CMEP) of the damage/yield function (Lorentz and Badel, 2004).

248 For details concerning their implementation, the interested reader is referred to example files made available on the
249 Cast3M website (<http://www-cast3m.cea.fr>).⁴

250 *4.1. Control by nodal displacement increment (CNDI)*

251 The CNDI criterion specifies that the increment of the linear combination of the displacements computed at a given
252 set of nodes equals $\Delta\tau$.

253 From De Borst (1987), the path-following constraint equation is written as:

$$p^{k+1} = \mathbf{p}^\top \Delta \mathbf{d}^{k+1} - \Delta\tau = 0 \quad (35)$$

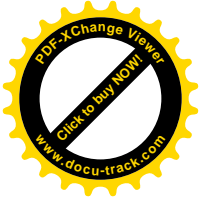
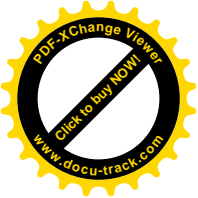
254 where \mathbf{p} is a selection vector containing the multiplication factors for the corresponding DOFs, and:

$$\Delta \mathbf{d}^{k+1} = \Delta \mathbf{d}^k + \delta \mathbf{d}_I^{k+1} + \delta \eta^{k+1} \delta \mathbf{d}_{II}^{k+1} \quad (36)$$

255 Since eq. (35) is linear in $\delta \mathbf{d}^{k+1}$, the value of $\delta \eta^{k+1}$ can be expressed as:

$$\delta \eta^{k+1} = \frac{\Delta\tau - a_0}{a_1} \quad (37)$$

⁴Files: `pilotage_indirect.1.dgibi` and `pilotage_indirect.2.dgibi`.



Listing 4: Syntax for adding user-defined constraint equations at the beginning of a Cast3M input file without changing the source code. Note (according to Cast3M keywords): 'CHPOINT' stands for point-wise field (nodal field in this case), 'FLOTTANT' stands for floating number.

```

* USER-DEFINED PROCEDURE *****
*****
* Beginning of the user procedure
* Input:
*   Info on geometry, materials, models (PRECED)
*   Displacement at previous time step (DEPT)
*   Displ. var. at iteration k (DU)
*   Displ. increment I at iteration k+1 (DUI)
*   Displ. increment II at iteration k+1 (DUII)
*   Path step length (DTAU)
'DEBPROC' PILOINDI
  PRECED      *'TABLE'
  U           *'CHPOINT'
  DU          *'CHPOINT'
  DUI         *'CHPOINT'
  DUII        *'CHPOINT'
  DTAU        *'FLOTTANT';
*****
* Solution of the user-defined path-following
* constraint equation
...
...
*****
* End of the user procedure
* Output: load multiplier variation (D_ETA)
'FINPROC' D_ETA ;
*****

```

256 where coefficients a_0 and a_1 are defined as:

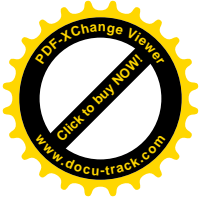
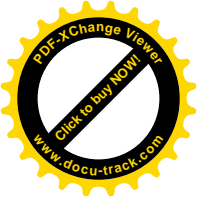
$$a_0 = \mathbf{p}^\top (\delta \mathbf{d}_I^{k+1} + \Delta \mathbf{d}^k) \tag{38}$$

$$a_1 = \mathbf{p}^\top \delta \mathbf{d}_I^{k+1} \tag{39}$$

257 Using Equation (37), it is possible to obtain the value of $\delta \eta^{k+1}$ both in the prediction and correction phase. For the
 258 prediction phase ($k + 1 = 1$), eq. (37) can be used with $\Delta \mathbf{d}^k = \Delta \mathbf{d}^0 = \mathbf{0}$. During computations, $\delta \mathbf{d}_I^{k+1}$ becomes
 259 smaller with each passing iteration (it is calculated from the unbalanced forces at the k -th iteration), whereas $\Delta \mathbf{d}^k$
 260 tends to stay stationary. Since the quantity $\delta \mathbf{d}^{k+1}$ is always different from zero, this implies that the value of $\delta \eta^{k+1}$
 261 should get ever closer to zero. This means that $\mathbf{p}^\top \Delta \mathbf{d}^{k+1}$ gets, in turn, ever closer to $\Delta \tau$, thus satisfying eq. (35).

262 *4.2. Controlling the maximum elastic predictor (CMEP)*

263 The effectiveness of the CNDI technique depends on whether the chosen combination of DOFs increases monotonically
 264 throughout the simulation. Unfortunately, finding a set of DOFs with this characteristic is not an easy task for
 265 general structures. That's why the CMSI formulation is chosen as default.



266 Although the CMSI approach can be applied to various situations, some studies indicate that it doesn't distinguish
267 between dissipative and non-dissipative (i.e., elastic unloading) solutions.

268 Path-following equations based on the maximization of the elastic predictor of the damage/plasticity function (i.e., the
269 value of the damage/yield criterion function when considering an incrementally elastic response) (Lorentz and Badel,
270 2004) can overcome this limitation, though this is achieved at the cost of a more intrusive and model-dependent
271 implementation.

272 4.2.1. Formulation

273 A path-following CMEP of the damage criterion function turns out to be well suited to capture localized dissipative
274 phenomena resulting from strain localization.

275 *Dissipative model.* As an example, we may assume that the material behaves according to a rate-independent con-
276 stitutive model with a single internal variable κ . Its evolution satisfies the Karush-Kuhn-Tucker and consistency
277 conditions:

$$f \leq 0 \quad \dot{\kappa} \geq 0 \quad \dot{\kappa}f = 0 \quad \dot{\kappa}\dot{f} = 0 \quad (40)$$

278 where $f = f(Y, \kappa)$ is a damage (plastic) criterion function and $Y = Y(\epsilon, \kappa)$ is the thermodynamic force associated
279 with κ .

280 *Constraint equation function.* According to Lorentz and Badel (2004), the constraint equation is expressed as in
281 eq. (26), with:

$$g_\alpha^{k+1} = f_\alpha^{\text{elas},k+1} \quad (41)$$

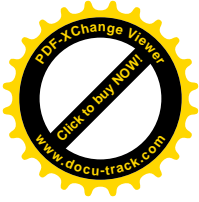
282 where the elastic predictor of the damage/plasticity criterion function is expressed as:

$$f_g^{\text{elas},k+1} = f(Y_\alpha(\epsilon_\alpha^{k+1}, \kappa_n), \kappa_n) \quad (42)$$

283 with κ_n standing for the internal variable at pseudo-time step t_n . Moreover:

$$\epsilon_\alpha^{k+1} = \mathbf{B}_\alpha(\mathbf{d}_n + \Delta\mathbf{d}^k + \delta\mathbf{d}_I^{k+1} + \delta\eta^{k+1}\delta\mathbf{d}_{II}^{k+1}) \quad (43)$$

284 As shown by Lorentz and Badel (2004), a positive value for the elastic predictor is associated with a dissipative branch
285 of the equilibrium path. For more details on the properties of the CMEP method, the interested reader can turn to said
286 paper.



287 *Resolution.* Since f_α is commonly chosen to be a convex function of ϵ_α , f_α^{elas} is also convex. Furthermore, given the
 288 convexity of the “max” function, the path-following constraint (41) preserves this same property. As a consequence,
 289 it may admit up to two distinct real or complex (inadmissible) roots. Their direct determination is, however, often
 290 impossible because the f_α^{elas} function is generally nonlinear, and the “max” operator represents an additional source
 291 of non-linearity.

292 As mentioned in previous sections, a possible solution strategy may be to use a “nested interval algorithm”. For this
 293 purpose, the elastic predictor function is linearized based on a known value of $\delta\eta$. The most straightforward choice
 294 consists in using an explicit solution procedure to avoid further local sub-iterations.

295 In that case, the f_α^{elas} function is linearized based on $\delta\eta^{k+1} = 0$ (i.e., about η^k) as:

$$f_\alpha^{\text{elas},k+1} = (f_\alpha^{\text{elas}})_{\delta\eta=0} + \left(\frac{\partial f_\alpha^{\text{elas}}}{\partial(\delta\eta)} \right)_{\delta\eta=0} \delta\eta^{k+1} \quad (44)$$

296 where:

$$(f_\alpha^{\text{elas}})_{\delta\eta=0} = f(Y_\alpha(\mathbf{B}_\alpha(\mathbf{d}_n + \Delta\mathbf{d}^k + \delta\mathbf{d}_1^{k+1}), \kappa_n), \kappa_n) \quad (45)$$

297 The constraint equation thus reads once again like (30), where coefficients $a_{0,\alpha}$ and $a_{1,\alpha}$ can be easily identified after
 298 computing $\partial f_\alpha^{\text{elas}} / \partial(\delta\eta)$.

299 *An example.* We may consider a simple isotropic continuum damage model where the damage criterion function can
 300 be expressed as:

$$f = \tilde{\epsilon} - \kappa \quad (46)$$

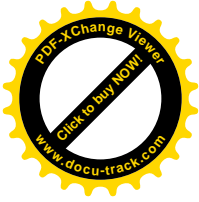
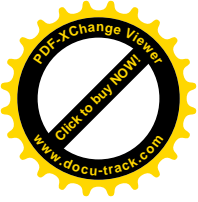
301 where $\tilde{\epsilon}$ is an equivalent strain measure.

302 Here, we consider the so-called Mazars (1984) equivalent strain, $\tilde{\epsilon} = \sqrt{\langle \epsilon_p \rangle \cdot \langle \epsilon_p \rangle}$, with $\langle \epsilon_p \rangle$ the positive part of the
 303 principal strain tensor (represented in vector format), and κ is the historical maximum of the equivalent strain.

304 The idea is to ensure that the elastic predictor function is equal to $\Delta\tau > 0$ on at least one integration point $\alpha \in \Omega^h$
 305 for each time step. The integration point α that serves as the basis for calculating the criterion is chosen automatically
 306 during iterations. To achieve this, the elastic predictor of the damage criterion function is defined for each integration
 307 point α :

$$f_\alpha^{\text{elas},k+1} = \tilde{\epsilon}_\alpha^{k+1} - \kappa_{\alpha,n} \quad (47)$$

308 where $\kappa_{\alpha,n}$ is the maximum equivalent strain experienced up to the beginning of the current time step.



309 The $a_{1,\alpha}$ and $a_{0,\alpha}$ factors can be computed by linearizing eq. (47) with respect to the unknown variable $\delta\eta$, from
 310 which:

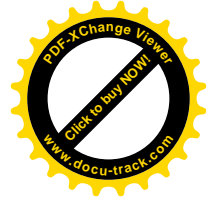
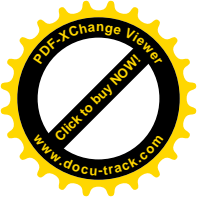
$$\begin{aligned} a_{0,\alpha} &= (f_\alpha^{\text{elas}})_{\delta\eta=0} \\ &= \left[\mathbf{G}_{\alpha,I}^{k+1} \mathbf{R}_{\alpha,I}^{k+1} \mathbf{B}_\alpha (\mathbf{d}^k + \delta \mathbf{d}_I^{k+1}) \right. \\ &\quad \left. \cdot \mathbf{G}_{\alpha,I}^{k+1} \mathbf{R}_{\alpha,I}^{k+1} \mathbf{B}_\alpha (\mathbf{d}^k + \delta \mathbf{d}_I^{k+1}) \right]^{1/2} - \kappa_{\alpha,n} \end{aligned} \quad (48)$$

311 and

$$\begin{aligned} a_{1,\alpha} &= \left(\frac{\partial f_\alpha^{\text{elas}}}{\partial (\delta\eta)} \right)_{\delta\eta=0} = \left(\frac{\partial \tilde{\varepsilon}_\alpha}{\partial (\delta\eta)} \right)_{\delta\eta=0} \\ &= \left(\left(\frac{\partial \tilde{\varepsilon}_\alpha}{\partial \langle \boldsymbol{\epsilon}_{\alpha,p} \rangle} \right)^\top \frac{\partial \langle \boldsymbol{\epsilon}_{\alpha,p} \rangle}{\partial \boldsymbol{\epsilon}_{\alpha,p}} \frac{\partial \boldsymbol{\epsilon}_{\alpha,p}}{\partial \boldsymbol{\epsilon}_\alpha} \frac{\partial \boldsymbol{\epsilon}_\alpha}{\partial (\delta\eta)} \right)_{\delta\eta=0} \\ &= \frac{\langle \boldsymbol{\epsilon}_{\alpha,p}^k \rangle^\top}{\tilde{\varepsilon}_\alpha^k} \mathbf{G}_\alpha^k \mathbf{R}_{\alpha,II}^{k+1} \mathbf{B}_\alpha \delta \mathbf{d}_{II}^{k+1} \end{aligned} \quad (49)$$

312 where $\mathbf{G}_{\alpha,I}^{k+1}$ is a diagonal matrix such that $G_{\alpha,I,ii}^{k+1} = 1$ if $(\mathbf{R}_{\alpha,I}^{k+1} \mathbf{B}_\alpha (\mathbf{d}^k + \delta \mathbf{d}_I^{k+1}))_i$ is positive and $G_{\alpha,I,ii}^{k+1} = 0$
 313 otherwise; \mathbf{G}_α^k is such that $G_{\alpha,ii}^k = 1$ if $\epsilon_{\alpha,p,i}^k$ is positive and $G_{\alpha,ii}^k = 0$ otherwise; and $\mathbf{R}_{\alpha,I}^{k+1}$ and $\mathbf{R}_{\alpha,II}^{k+1}$ are the
 314 matrices that rotate the strains $\mathbf{B}_\alpha (\mathbf{d}^k + \delta \mathbf{d}_I^{k+1})$ and $\mathbf{B}_\alpha \delta \mathbf{d}_{II}^{k+1}$ into their respective principal basis.⁵

⁵Alternatively, one could have replaced $\mathbf{R}_{\alpha,I}^{k+1}$ and $\mathbf{R}_{\alpha,II}^{k+1}$ by \mathbf{R}_α^k , the rotation matrix of the strain vector at iteration k into its principal basis.



315 5. Performance assessment

316 The performance of the implementation proposed herein is assessed through a simple three-point bending test for
317 which a stable global response is obtained. This allows for a direct comparison between the standard iterative New-
318 ton solver and the path-following solver (with different constraint equations) in terms of CPU times and number of
319 iterations needed to converge.

320 All performed simulations use the elastic stiffness operator to compute \mathbf{K}^k in conjunction with convergence acceler-
321 ation (default choice in Cast3M). Of course, the use of other stiffness tensors could affect the convergence properties
322 of the proposed methods. Notice, however, that no additional constraints are created by the studied path-following
323 methods on the iterative strategy and on the choice of this operator.

324 5.1. Constitutive assumptions and damage regularization

325 In this example, as well as in the examples illustrated in the next section, the regions that must remain intact through-
326 out the analysis are modeled using an isotropic linear elastic constitutive model. The isotropic continuum damage
327 mechanics model from Mazars (1984) is used for areas susceptible to damage.⁶

328 It is well known that softening material models lead to mesh-dependent results when used with a finite element
329 method. In such cases, the structural dissipation becomes dependent on the mesh size and may eventually become
330 smaller as the mesh size decreases. For these models, regularization methods (see, among others, Hillerborg et al.
331 (1976), Peerlings et al. (1998), Giry et al. (2011), Rastiello et al. (2018)) are generally adopted in order to generate
332 mesh-independent results. In this study, no regularization techniques are used, both for the sake of simplicity and in
333 order to induce sharp snap-backs (see next section). However, the path-following strategies presented herein can be
334 used with regularized models without significant modifications.

335 5.2. Three-point bending test

336 5.2.1. Problem setting

337 Here, a notched beam submitted to a three-point bending test is considered. The geometry and boundary conditions
338 are defined in fig. 3. The elements between the notch and the upper horizontal boundary are supposed damageable,
339 whereas a linear elastic material behavior is assumed for the other elements. The material parameters used in these
340 computations (table 1) have been selected to generate a stable response (i.e., without snap-back) in the post-load peak
341 phase.

⁶This constitutive law was selected because it is a popular choice for modeling damage of quasi-brittle materials. Other constitutive equations may, of course, be considered.

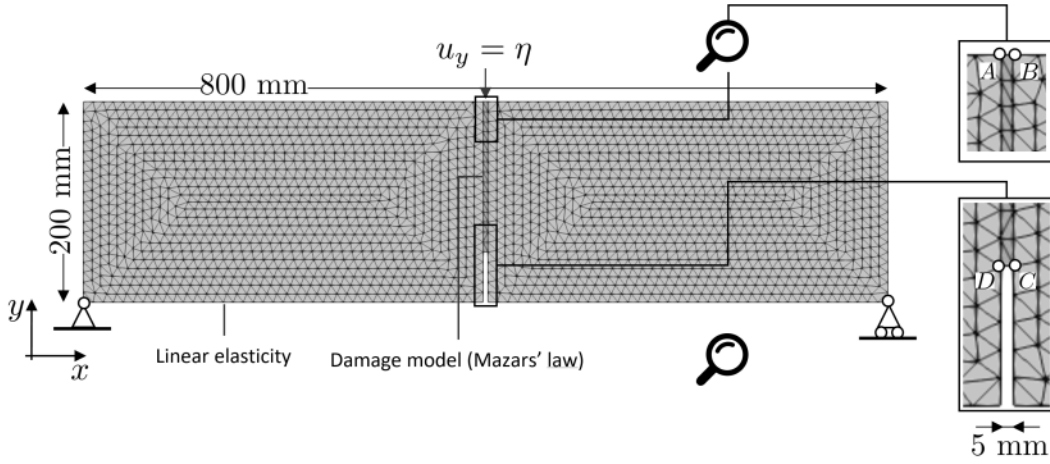


Figure 3: Three-point bending test – geometry and boundary conditions.

342 A reference simulation is performed by applying a vertical displacement (Direct Dirichlet Condition, DDC) to the
 343 bearing surface (nodes A and B in fig. 3), and increasing its value. The response obtained in this manner is then
 344 compared with the responses obtained using the path-following strategies.

345 5.2.2. Constraint equations

346 The path-following solver is set up so as to replicate the global responses of the DDC simulation. In particular, the
 347 CNDI and CMSI formulations are used as follows:

348 **CNDI-top.** The CNDI algorithm is used to replicate the directly-imposed displacement boundary condition. The
 349 constraint equation controls the vertical displacement of nodes A and B (fig. 3):

$$p^{k+1} = -\frac{\Delta d_{y,A}^{k+1} + \Delta d_{y,B}^{k+1}}{2} - \Delta\tau = 0 \quad (50)$$

350 where $d_{y,\bullet}$ ($\bullet = A, B$) is the vertical component of vector \mathbf{d} at node \bullet and $\Delta\tau > 0$.

351 **CNDI-cmod.** The CNDI algorithm is then used to control the Crack Mouth Opening displacement at the notch, i.e.:

$$p^{k+1} = \Delta d_{x,C}^{k+1} - \Delta d_{x,D}^{k+1} - \Delta\tau = 0 \quad (51)$$

352 where $d_{x,\bullet}$ ($\bullet = C, D$) is the horizontal component of \mathbf{d} at node \bullet . In order to ensure a proper comparison, the
 353 simulation is performed with exactly the same number of loading steps as the reference simulation. Moreover,
 354 the $\Delta\tau$ parameter is not supposed constant but is defined by the variations of $\Delta d_{x,C}^{k+1} - \Delta d_{x,D}^{k+1}$ recorded during
 355 the DDC simulation (fig. 4).

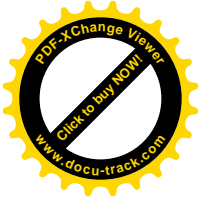
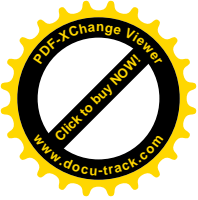


Table 1: Material constants of Mazars’ model. Numerical values selected for simulating a three-point bending test without snap-backs.

Parameter	Description	Value
ν	Poisson’s ratio	0.15
E	Young modulus	30 GPa
ρ	Density	2300 kg/m ³
ε_0	Damage initiation threshold	1.0×10^{-5}
A_t	Mazars’ model input	0.2
A_c	Mazars’ model input	1.2
B_t	Mazars’ model input	0.8×10^3
B_c	Mazars’ model input	1.5×10^3
β	Mazars’ model input	1.06

356 **CMSI.** Finally, the CMSI algorithm is applied. Once again, the $\Delta\tau$ parameter varies with $\max_{\Omega^h}(\mathbf{q}_\alpha^\top \Delta\epsilon_\alpha^{k+1})$, which
 357 was recorded during the standard Newton solver simulation. The number of loading steps used is, again, exactly
 358 the same as in the DDC simulation.

359 As shown in fig. 4, these choices yield the same global force-displacement response as the one obtained with the DDC
 360 simulation.

361 5.2.3. Performance assessment

362 The comparison between Newton and path-following solvers is performed in terms of the total time spent on the
 363 iterative solving process (t_{it}) and the time spent on solving the constraint equation (t_{pf}). Time t_{it} includes any time
 364 spent, over the iterations, on assembling the matrices, imposing boundary conditions, solving the linear systems and
 365 updating the solution. Accordingly, the total time spent running the simulation is $t_{tot} = t_{it} + t_{pf}$.

366 For a proper comparison, each simulation is repeated 5 times in order to average the values of t_{it} and t_{pf} . As shown
 367 in fig. 5:

- 368 • t_{pf} is always very small compared to t_{it} . As expected, t_{pf} is larger for the CMSI method than for the CNDI
 369 formulations because of the nested interval algorithm. This CPU time can be reduced by limiting the resolution
 370 of the constraint equation exclusively to the part of the mesh likely to experience damage.
- 371 • t_{tot} is very similar for all direct/indirect ways of imposing Dirichlet boundary conditions. The time spent
 372 solving the equilibrium problem is quite stable despite the fact that with path-following solvers, each global
 373 iteration requires two computations of the linear system. This can easily be explained in light of the results

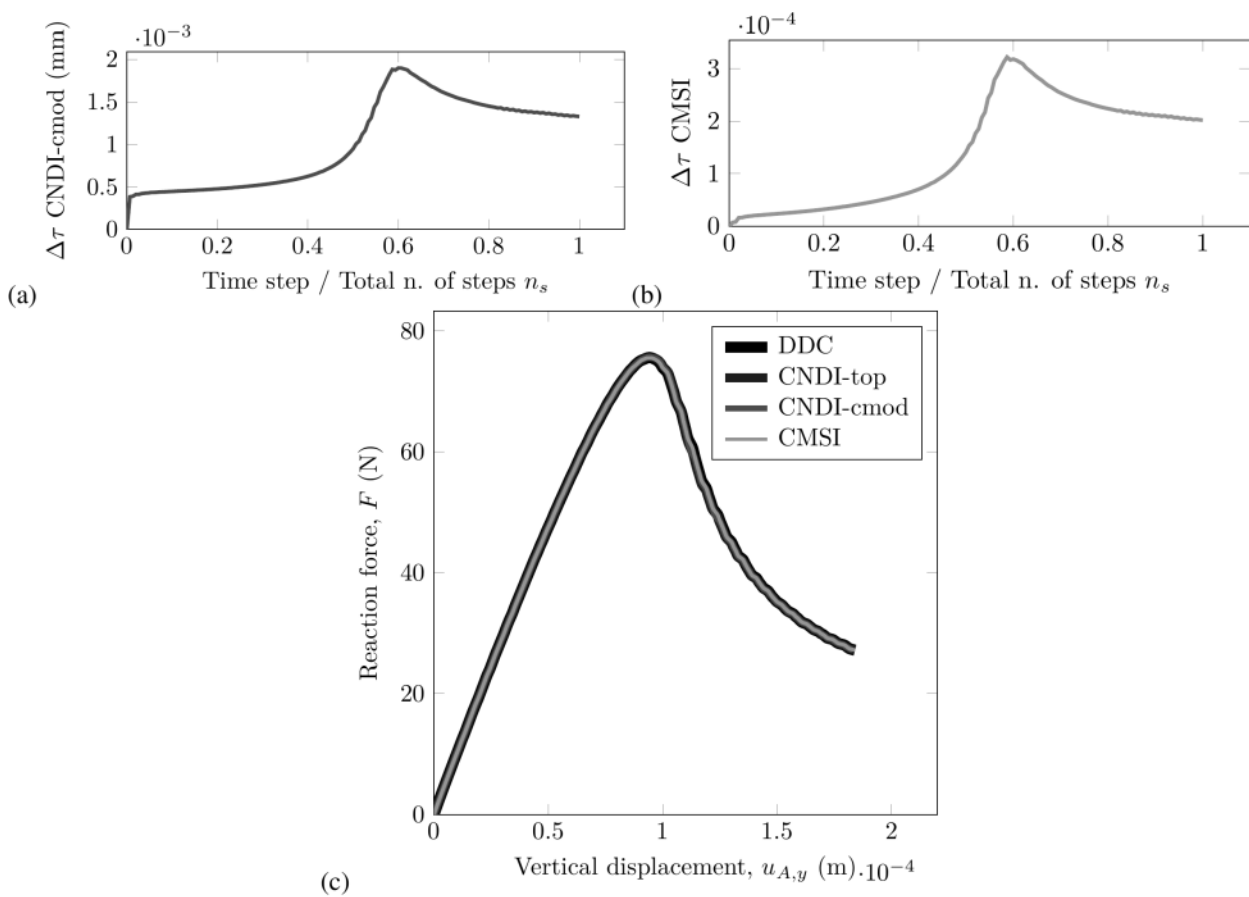


Figure 4: Three-point bending test – (a) Prescribed variation of the path step length in the CNDI-cmod computation as a function of time, (b) Prescribed variation of the path step length in the CMSI computation as a function of time, and (c) Global responses.

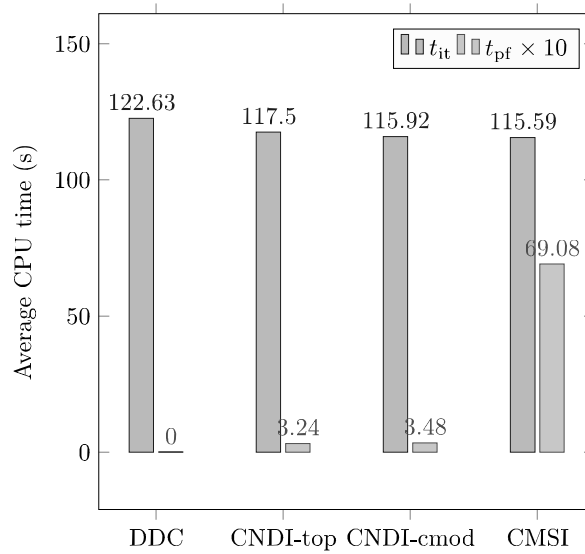
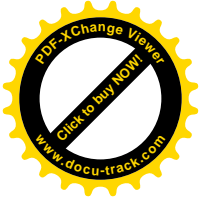
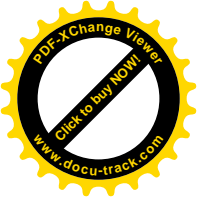


Figure 5: Three-point bending test – Average CPU times (a scale factor of 10 is applied to t_{pf} for clarity).

374 depicted in fig. 6, which represents the evolution of the number of iterations per pseudo-time step. These curves
375 clearly show that the number of iterations required by the path-following solvers is generally half less than what
376 is required by the Newton solver to achieve convergence. In other words, convergence is accelerated. Of course,
377 more studies will be needed to better explain these results, but the trend is clear for all the constraint equations
378 considered.

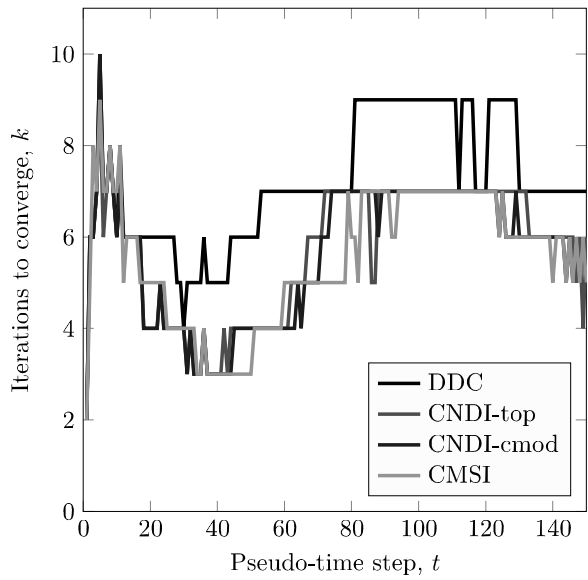
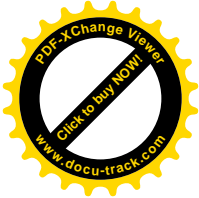
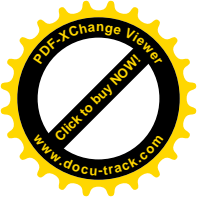


Figure 6: Three-point bending test – Number of iterations required for convergence.

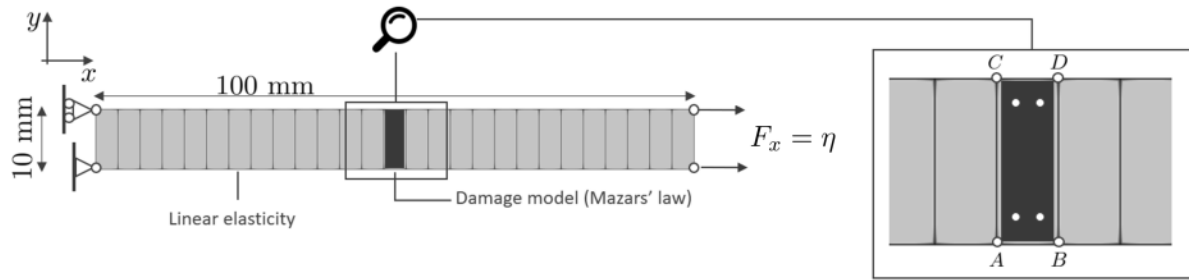


Figure 7: Beam under tension – geometry and boundary conditions.

379 6. Numerical examples with sharp snap-back responses

380 Three test cases are considered in order to show the convergence and stability of the proposed numerical framework.
 381 The problems considered are 2D and 3D, but the proposed framework also works in a one-dimensional (1D) context.
 382 However, this case is not considered here as it is pretty trivial compared with 2D and 3D simulations.

383 6.1. 2D beam under tensile loading (indirectly-controlled force)

384 The first test case simulates a tensile load on a 2D beam. This test was chosen because it is often used to study mesh
 385 sensitivity when using strain-softening constitutive models (see, e.g., Giry et al. (2011), Rastiello et al. (2018)).

386 6.1.1. Problem setting

387 The structure consists of two elastic regions connected by an intermediate damageable zone where strain localization
 388 occurs. The geometry and boundary conditions are illustrated in fig. 7. The beam's left side is constrained, while
 389 loading is applied under indirect force control by pulling on the beam's right side. Plane stress conditions are assumed.

390 The finite element discretization Ω^h is obtained using linear quadrilateral finite elements (QUA4). Several mesh
 391 refinement levels are considered to study the algorithm's capability to capture pronounced snap-back responses as the
 392 damaging band gets thinner. The number of finite elements along the longitudinal direction is denoted n . Its values
 393 range from 3 to 29 in order to obtain structural responses that are increasingly unstable. Alternatively, one could have
 394 chosen a fixed size for the damaging element and increased the beam's length progressively.

395 The material parameters used in the computations are given in Table 2. The same parameters will be used for all the
 396 examples described in this section.

397 6.1.2. Discussion

398 An equilibrium path is obtained for each criterion proposed previously. In particular, the CNDI method is applied to
 399 control the relative horizontal displacement of nodes B and A , i.e.:

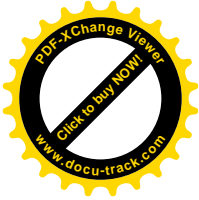
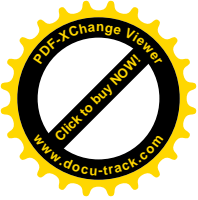


Table 2: Material constants of Mazars' model. Numerical values selected for the numerical examples.

Parameter	Description	Value
ν	Poisson's ratio	0
E	Young modulus	1 GPa
ρ	Density	2300 kg/m ³
ε_0	Damage initiation threshold	1.0×10^{-4}
A_t	Mazars' model input	1.0
A_c	Mazars' model input	1.2
B_t	Mazars' model input	1.0×10^4
B_c	Mazars' model input	1.5×10^3
β	Mazars' model input	1.06

$$p^{k+1} = \Delta d_{x,B}^{k+1} - \Delta d_{x,A}^{k+1} - \Delta\tau = 0 \quad (52)$$

400 where $d_{x,\bullet}$ ($\bullet = A, B$) is the horizontal component of the displacement vector \mathbf{d} at node \bullet and $\Delta\tau > 0$. Moreover,
401 the CMSI and CMEP methods were applied by restricting the constraint equation to the set of finite elements where
402 damage is expected to vary.

403 The simplicity of the geometry and the boundary conditions ensures that the three path-following criteria considered
404 provide precisely the same force-displacement responses. However, the CMEP formulation presents a significant
405 difference with the other criteria: it is possible to reach the peak of the local stress-strain law during the first load
406 increment. This feature is a clear advantage if the focus of the analysis is the post-peak trajectory, because it reduces
407 the calculation time.

408 Numerical results show that by successively increasing n from 3 to 29, the structural response becomes increasingly
409 unstable (fig. 8a). For $n = 3$ the area where the damage occurs is large enough to dissipate energy in a controlled
410 manner, so no snap-back is observed. However, when n increases, this region shrinks and loses its ability to dissipate
411 energy in a controlled way. This means that once the damage starts, new equilibrium solutions may only be found at
412 the cost of a simultaneous reduction in load and displacements. The severity of the snap-back reflects the intensity of
413 this effect.

414 Regarding the fulfillment of the path-following constraint equation, fig. 8b shows that the required value of $\Delta\tau$ is at-
415 tained at every time step until the end of the analysis, regardless of the chosen path-following equation. This indicates
416 that the proposed algorithm stays stable and convergent, even in the presence of severe instabilities. Moreover, the
417 proposed implementation can capture the complete equilibrium path.

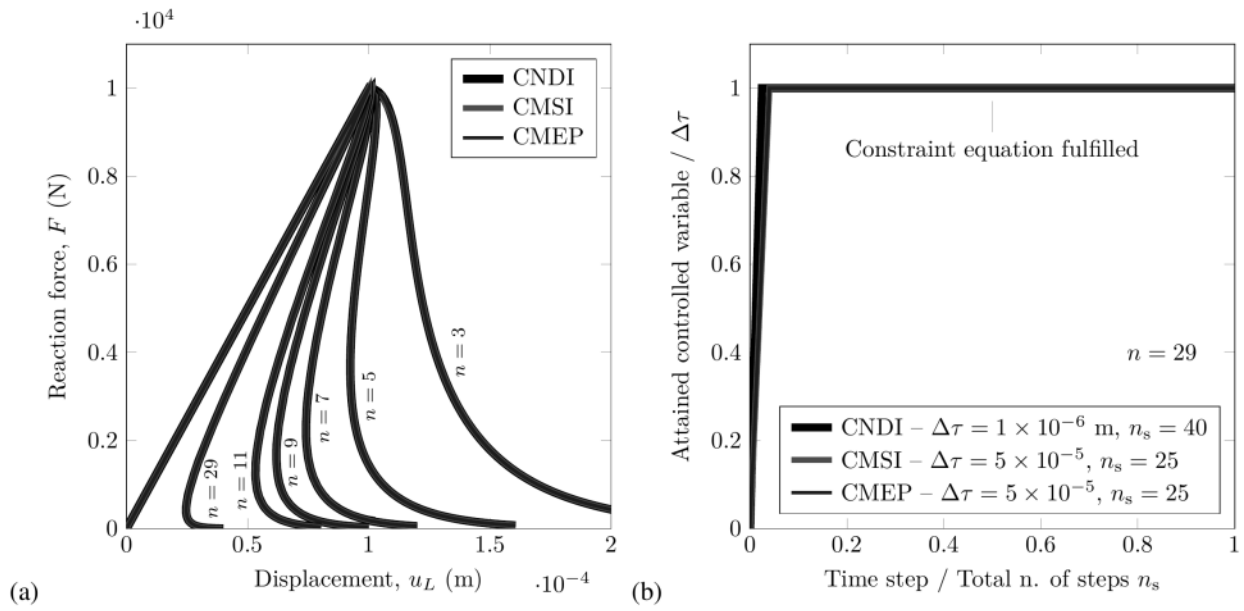


Figure 8: Beam under tension – Effect of damage localization on the global response. The occurrence of increasingly severe snap-backs reflects the intensity of the strain localization effects. The value of the constraint equation is checked throughout the analysis for each criterion used.

6.2. 2D notched beam under tensile loading (indirectly-controlled displacement)

The second 2D example is a traction test on a notched beam. This test case is quite close to the previous one. However, the presence of the two notches complexify the strain localization process since one may expect that damage will start at the notches and progressively propagate towards the center of the beam.

6.2.1. Problem setting

The geometry of the beam is given in fig. 9. The displacement is constrained at the left edge, whereas the load is applied at the right edge by imposing an indirectly-controlled displacement. Plane stress conditions are assumed.

A regular mesh Ω^h is used to discretize the computational domain for simplicity and to identify the localization zone clearly; more complex unstructured meshes can be used without significant modifications.

6.2.2. Selection of the controlled DOFs with the CNDI

In order to use the CNDI criterion, it is necessary to choose a set of DOFs to be controlled. This choice is generally made based on engineering or physical considerations regarding the expected damaging process. Alternatively, it can be made for the purpose of replicating experimental control techniques, e.g., when crack-opening displacements at given positions are controlled through Linear Variable Displacement Transducers (LVDTs).

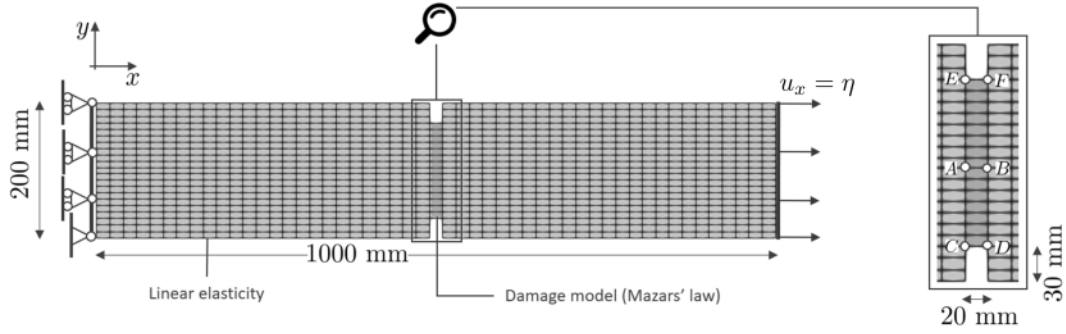


Figure 9: Tensile test on a notched beam – Geometry, boundary conditions and designation of the nodes considered for the application of the CNDI formulation.

432 Now, given the considered geometry and boundary conditions, the most relevant choice is to control the linear com-
 433 bination of the horizontal displacements of the nodes located on the vertical boundaries of each of the damage zones
 434 (Figure 9). In order to study the effects of such a choice, we considered:

435 **CNDI-1.** Two nodes (denoted *A* and *B*) located at mid-height of the beam. The variation of their relative displacement
 436 is controlled, i.e.:

$$p^{k+1} = \Delta d_{x,B}^{k+1} - \Delta d_{x,A}^{k+1} - \Delta \tau = 0 \quad (53)$$

437 **CNDI-2.** Two nodes located at the bottom notch. The Crack Mouth Opening Displacement (CMOD) variation at the
 438 bottom notch is controlled, i.e.:

$$p^{k+1} = \Delta d_{x,D}^{k+1} - \Delta d_{x,C}^{k+1} - \Delta \tau = 0 \quad (54)$$

439 **CNDI-3.** The mean value of the CMOD measures at the top and bottom notches, as is classically done in experiments,
 440 i.e.:

$$p^{k+1} = \frac{\Delta d_{x,D}^{k+1} - \Delta d_{x,C}^{k+1} + \Delta d_{x,F}^{k+1} - \Delta d_{x,E}^{k+1}}{2} - \Delta \tau = 0 \quad (55)$$

441 The results depicted in fig. 10 show that the choice of points on one notch exclusively (case CNDI-2) can lead to a loss
 442 of part of the equilibrium path. This occurs because damage originates at the notches, and because small numerical
 443 differences in CMOD are observed between the two notches during the simulation. Indeed, the CMOD at the top
 444 notch is found to be slightly larger than at the bottom one, which leads to the observed loss of part of the equilibrium
 445 path. However, in the subsequent phases of the simulation, the algorithm continues to follow the curve correctly.
 446 Moreover, this effect cannot be mitigated by controlling the displacement at both notches simultaneously using the
 447 average CMOD (case CNDI-3).

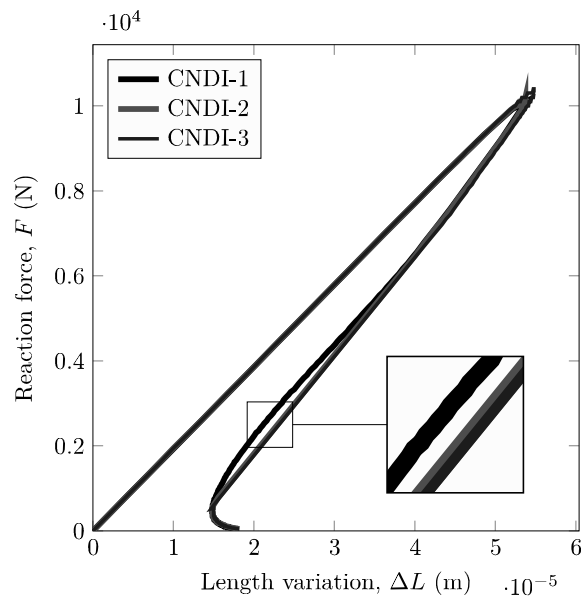


Figure 10: Tensile test on a notched bar – Comparison between the equilibrium paths obtained via CNDI for different base points.

448 On the other hand, no such limitation is found for a choice of points located in the middle of the ligament zone
 449 (case CNDI-1). This is because damage to the corresponding elements occurs late (at the end of the test). Over the
 450 course of the entire damage propagation process, these nodes experience a smaller relative displacement than the one
 451 experienced at notches. For this reason, the constraint eq. (53) is used for the comparison with the CMSI and CMEP
 452 formulations.

453 6.2.3. Discussion

454 As we already observed in the previous example, fig. 11a shows a good agreement between the force-displacement
 455 equilibrium curves computed using the three different path-following constraint equations. Moreover, for all of them,
 456 the values chosen for the variable $\Delta\tau$ are strictly respected throughout the simulations (fig. 11b).

457 Such a simultaneous reduction of force and displacement enables us to simulate a gradual damaging process (fig. 12).
 458 As expected, damage originates at both notches and progressively propagates towards the beam's center. As it pro-
 459 gresses, the structure's effective resisting area becomes smaller and so does the amount of energy that can be dissipated
 460 in a controlled manner. After reaching the peak load, new equilibrium points can only be found if there is a simulta-
 461 neous decrease in displacements and the external load.

462 Replicating such a gradual process would not have been possible without an indirect loading control method. One
 463 could have observed a sharp damage localization increase (from zero to one) on the beam's central part.

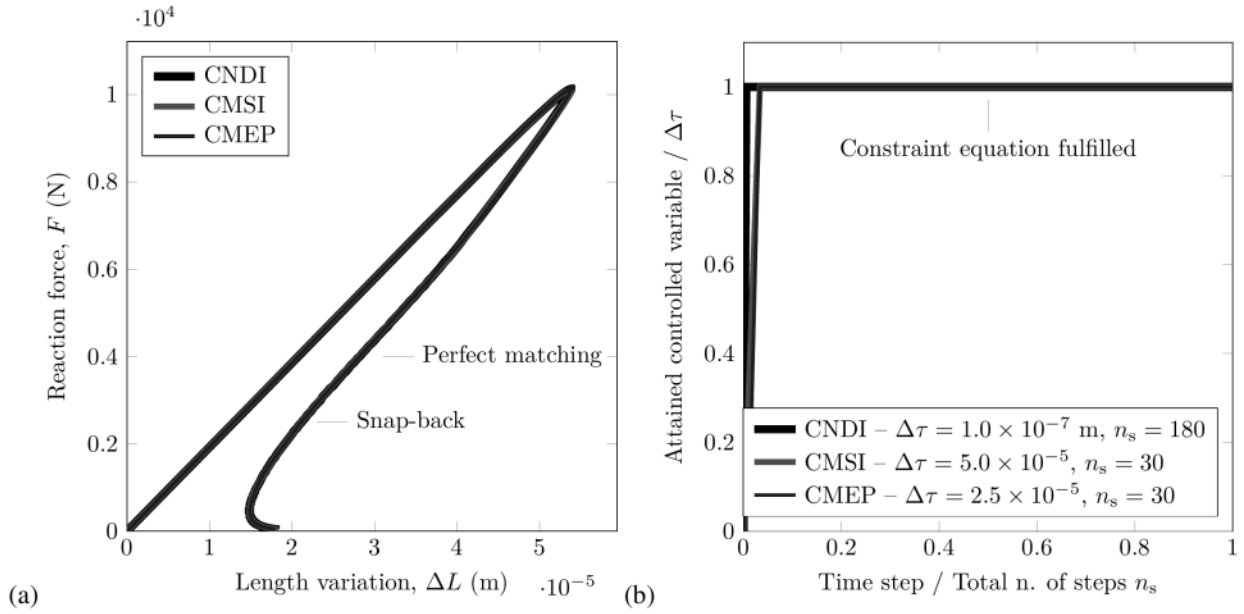


Figure 11: Tensile test on a notched bar – (a) Global force-displacement responses; (b) Fulfillment of the constraint equation.

464 6.3. 3D perforated plate under tensile loading (indirectly-controlled displacement)

465 The final simulation is a tensile test on an eccentrically-perforated plate. The center of the circular hole is located
 466 along the vertical symmetry axis of the plate but is distinct from the center of the plate. The two-dimensional version
 467 of this example can be found in the literature (see, e.g., Lorentz and Badel (2004), Rastiello et al. (2019)) and is
 468 typically simulated to test path-following algorithms in the case of structural responses characterized by multiple
 469 snap-back phases.

470 6.3.1. Problem setting

471 The 3D geometry of the plate is depicted in fig. 13. The analysis is carried out by applying indirectly-controlled
 472 displacements on the right boundary of the plate, whereas the left one is constrained (fig. 13a). The discretization of
 473 the computational domain is obtained through linear tetrahedral finite elements (fig. 13b).

474 6.3.2. Discussion

475 All three criteria illustrated in this study are tested. Following Rastiello et al. (2019), the CNDI formulation is used
 476 for controlling the average CMOD at the hole. Since two cracks are expected to propagate from the hole toward the
 477 upper and lower boundaries, it seems quite natural to select the controlled DOFs. Here, the constraint equation is
 478 written as follows:

$$p^{k+1} = \frac{\Delta d_{x,D}^{k+1} - \Delta d_{x,C}^{k+1} + \Delta d_{x,B}^{k+1} - \Delta d_{x,A}^{k+1}}{2} - \Delta\tau = 0 \quad (56)$$

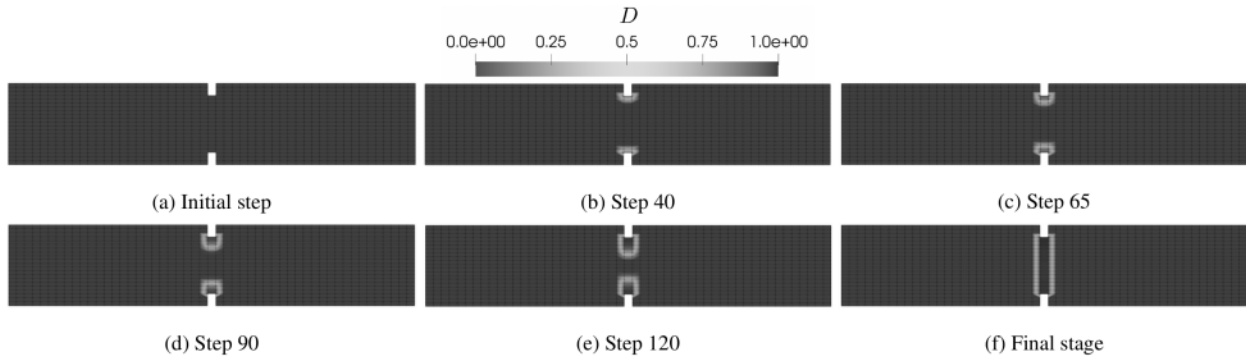


Figure 12: Tensile test on a notched bar – Damage progression during the simulation.

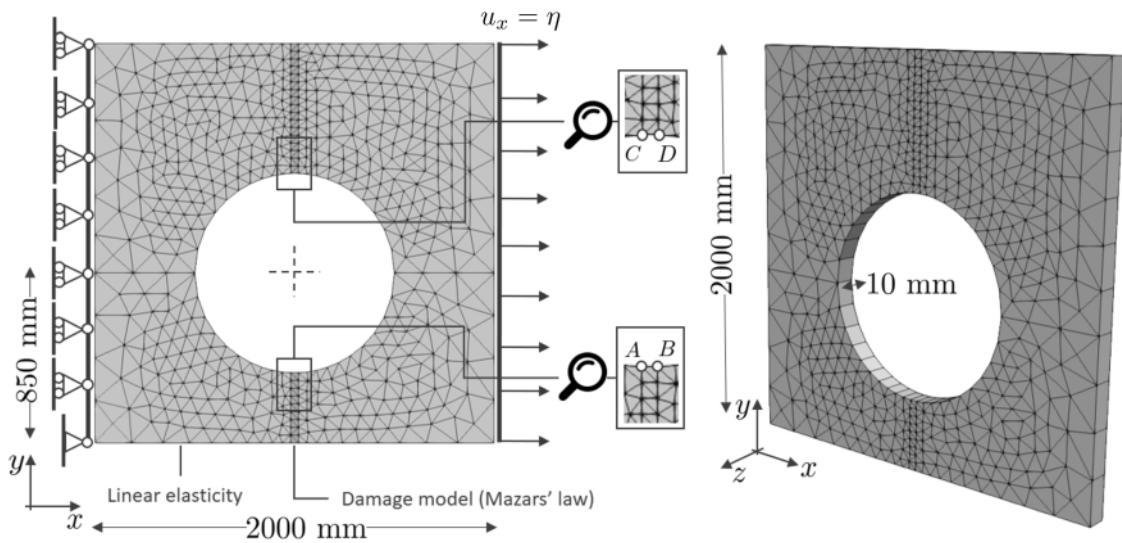


Figure 13: 3D perforated plate under tensile loading – Geometry and boundary conditions; Perspective view.

479 Numerical results (fig. 14a) show that the CNDI algorithm can predict the load peak and the existence of two snap-
 480 backs. However, it is unable to follow the equilibrium path smoothly. The reason for this is the choice of the
 481 reference points which guide the path-following equation. Conversely, the results obtained using the CMSI and
 482 CMEP formulations are in good agreement. In addition to predicting the peak load and the existence of the two snap-
 483 backs, they describe the entire equilibrium path all the way to the rupture. Remarkably, the proposed formulations
 484 provide solutions even in the presence of severe instabilities.

485 Figure 14b shows that the value of $\Delta\tau$ is attained with each criterion and for every analysis. However, convergence
 486 cannot be ensured when using the CNDI algorithm, in particular during the second snap-back phase. Notice that, as
 487 was already observed by Rastiello et al. (2019), the jump in the global response observed with the CNDI formula-
 488 tion (where the other methods instead predict the first snap-back) cannot be attributed to the non-fulfillment of the
 489 constraint equation. However, this is directly related to the controlled DOFs chosen. While the simulation ends prema-

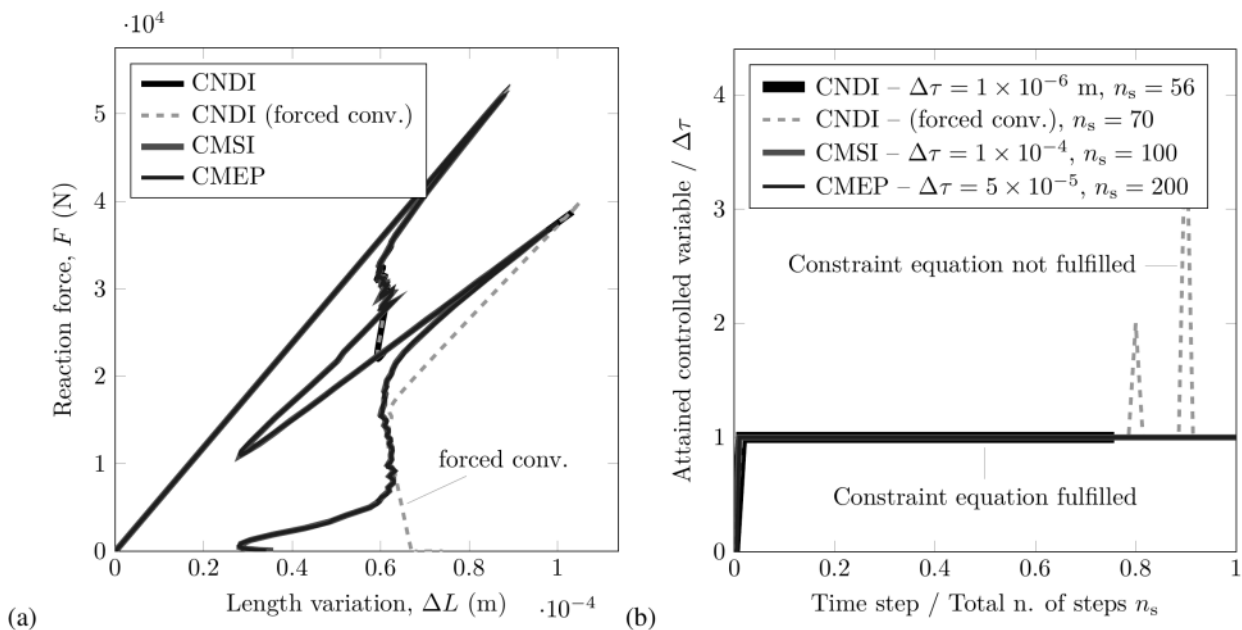


Figure 14: 3D holed plate under tensile loading – (a) Global force-displacement responses; (b) Fulfillment of the constraint equation.

490 purely with CNDI, this can be prevented by activating the “forced convergence” (a mixed implicit-explicit formulation
 491 in which the novel solution is predicted based on previous ones) feature in the Cast3M software (dashed green line).
 492 In that case, however, the constraint equation is not fulfilled a second time.

493 Observing the failure mechanism of this structure (fig. 15) is also quite interesting. In the linear phase, strain accu-
 494 mulates at the upper and lower edges of the circular hole until the maximum load is reached. Then, the local energy
 495 dissipation capacity is depleted and neighboring finite elements begin to be solicited. This process causes the strain
 496 localization to move. This first occurs in the plate’s lower ligament zone and corresponds to the occurrence of the first
 497 snap-back. The structure does not suddenly break; it can withstand increases in tension, but not for too long. A new
 498 strain concentration zone appears in the superior ligament, which generates the second snap-back, culminating in the
 499 rupture of the piece.

500 7. Conclusions

501 The present study proposes path-following methods for the finite element software Cast3M (Verpeaux et al., 1989),
 502 developed by the CEA (French Alternative Energies and Atomic Energy Commission, France) and freely distributed
 503 for research and educational purposes. This framework preserves the essence of the successful numerical methods in
 504 this field of study:

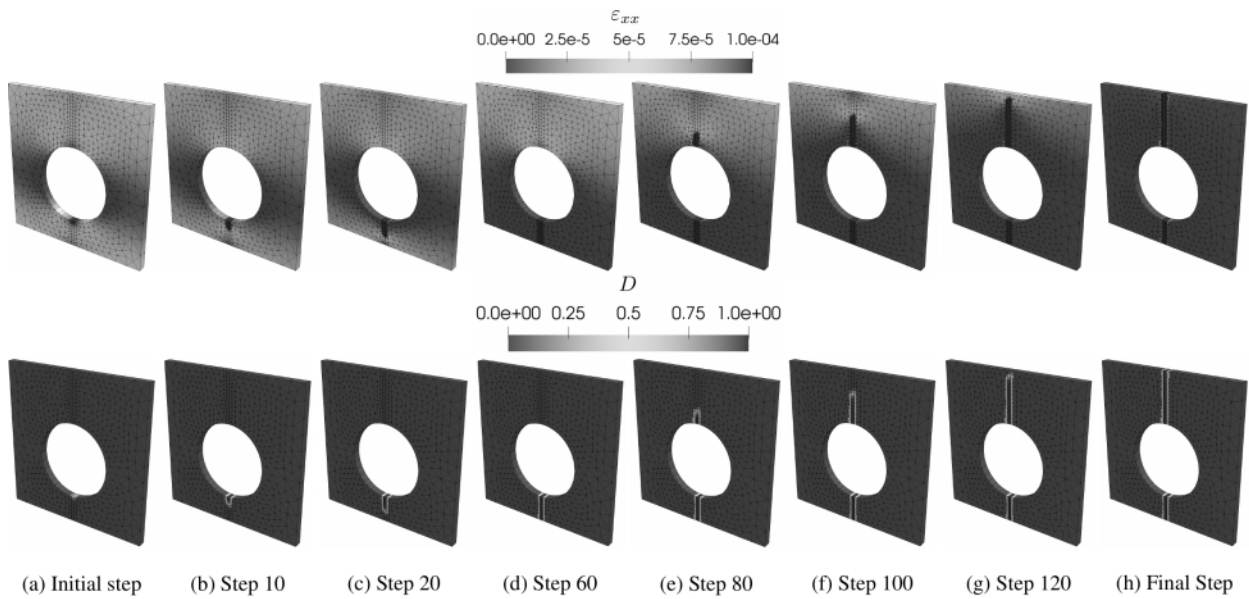


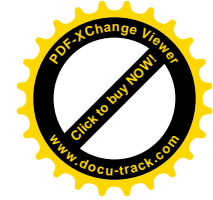
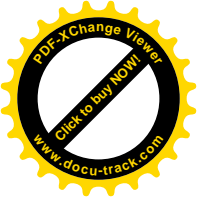
Figure 15: 3D holed plate under tensile loading – Horizontal strain (ϵ_{xx}) and damage field evolution.

- 505 (i) Breaking down the load into two components, one known and one unknown, the latter depending on an addi-
506 tional unknown: the load multiplier (Riks, 1979).
- 507 (ii) In a Newton-like solution process, breaking down the unknown displacement correction solution as the sum
508 of two contributions that can be determined from two linearized systems of equilibrium equations that are
509 independent of the load multiplier variation (Crisfield, 1983).
- 510 (iii) Determining the load multiplier variation from the solution of an additional equation of the problem: the path-
511 following constraint equation.

512 The framework has a modular and independent design in order to accommodate multiple path-following constraint
513 equations in a standalone way (i.e., without requiring modifications to the source code).

514 Three path-following equations were selected for implementation and testing: the control of the nodal displacement
515 increment (CNDI), the control of the maximum strain increment (CMSI), and the control of the maximum elastic pre-
516 dictor (CMEP) over the computational domain. The CMSI formulation is proposed as the default case because of its
517 general nature that makes it applicable to most situations regardless of the constitutive model. The other formulations
518 were implemented through a simple overload of the new PILOINDI procedure.

519 These three path-following constraint criteria were applied to simple 2D and 3D test cases involving strain localization.
520 The algorithm was found to be stable and convergent, even in the presence of severe snap-backs. The three methods
521 were able to predict the peak load and the existence of post-peak instabilities.



522 The proposed framework will prove particularly helpful in studies involving new path-following equations. As demon-
523 strated with the CNDI, CMSI, and CMEP criteria, the software users can focus on developing new path equations
524 tailored to their needs.

525 Finally, this study was limited to structural instabilities induced by a nonlinear material response. However, the
526 implementation proposed herein also works for geometrical nonlinearities, with the inclusion of large strains.

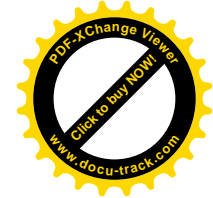
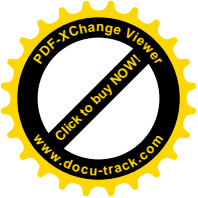
527 The developments presented in this paper are made available to the users/developers community along with Cast3M
528 2021 (release date: June 2021).

529 Acknowledgments

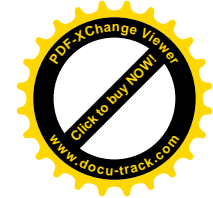
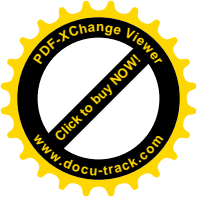
530 The authors declare that they have no known competing financial interests or personal relationships that could have
531 appeared to influence the work reported in this paper.

532 References

- 533 G. Alfano and M. A. Crisfield. Solution strategies for the delamination analysis based on a combination of local-control arc-length and line
534 searches. *International Journal for Numerical Methods in Engineering*, 58(7):999–1048, 2003. ISSN 1097-0207. doi: 10.1002/nme.806.
- 535 I. Babuška. The finite element method with lagrangian multipliers. *Numerische Mathematik*, 20(3):179–192, 1973.
- 536 E. Barbieri, F. Ongaro, and N. M. Pugno. A j-integral-based arc-length solver for brittle and ductile crack propagation in finite deformation-finite
537 strain hyperelastic solids with an application to graphene kirigami. *Computer Methods in Applied Mechanics and Engineering*, 315:713 – 743,
538 2017. ISSN 0045-7825. doi: <https://doi.org/10.1016/j.cma.2016.10.043>.
- 539 Z. P. Bažant. Structural stability. *International Journal of Solids and Structures*, 37(1-2):55–67, 2000.
- 540 D. Bellora and R. Vescovin. Hybrid geometric-dissipative arc-length methods for the quasi-static analysis of delamination problems. *Computers
541 & Structures*, 175:123–133, 2016.
- 542 A. Bilotta, L. Leonetti, and G. Garcea. An algorithm for incremental elastoplastic analysis using equality constrained sequential quadratic pro-
543 gramming. *Computers & structures*, 102:97–107, 2012.
- 544 B. Brank, A. Stanić, and A. Ibrahimbegovic. A path-following method based on plastic dissipation control. In *Computational Methods for Solids
545 and Fluids*, pages 29–47. Springer, 2016.
- 546 F. Cazes, G. Meschke, and M.-M. Zhou. Strong discontinuity approaches: An algorithm for robust performance and comparative assessment of ac-
547 curacy. *International Journal of Solids and Structures*, 96:355 – 379, 2016. ISSN 0020-7683. doi: <https://doi.org/10.1016/j.ijsostr.2016.05.016>.
- 548 Z. Chen and H. L. Schreyer. A numerical solution scheme for softening problems involving total strain control. *Computers & Structures*, 37(6):
549 1043–1050, 1990.
- 550 M. Crisfield. An arc-length method including line searches and accelerations. *International journal for numerical methods in engineering*, 19(9):
551 1269–1289, 1983.
- 552 M. A. Crisfield. A fast incremental/iterative solution procedure that handles snap-through. *Computers & Structures*, 13(1-3):55–62, 1981.
- 553 R. De Borst. Computation of post-bifurcation and post-failure behavior of strain-softening solids. *Computers & Structures*, 25(2):211–224, 1987.
- 554 R. De Borst, M. A. Crisfield, J. J. C. Remmers, and C. V. Verhoosel. *Nonlinear finite element analysis of solids and structures*. John Wiley & Sons,
555 2012.
- 556 L. Ebersolt, A. Combescure, A. Millard, and P. Verpeaux. Non-linear algorithms solved with the help of the gibiane macro-language. In *Transac-
557 tions of the 9th international conference on structural mechanics in reactor technology. Vol. B*, 1987.



- 558 G. Formica, V. Sansalone, and R. Casciaro. A mixed solution strategy for the nonlinear analysis of brick masonry walls. *Computer Methods in*
559 *Applied Mechanics and Engineering*, 191(51):5847–5876, 2002. ISSN 0045-7825. doi: [https://doi.org/10.1016/S0045-7825\(02\)00501-7](https://doi.org/10.1016/S0045-7825(02)00501-7). URL
560 <https://www.sciencedirect.com/science/article/pii/S0045782502005017>.
- 561 G. Garcea, G. A. Trunfio, and R. Casciaro. Mixed formulation and locking in path-following nonlinear analysis. *Computer Methods in Ap-*
562 *plied Mechanics and Engineering*, 165(1):247–272, 1998. ISSN 0045-7825. doi: [https://doi.org/10.1016/S0045-7825\(98\)00068-1](https://doi.org/10.1016/S0045-7825(98)00068-1). URL
563 <https://www.sciencedirect.com/science/article/pii/S0045782598000681>.
- 564 M. G. D. Geers. Enhanced solution control for physically and geometrically non-linear problems. Part I – the subplane control approach. *Interna-*
565 *tional Journal for Numerical Methods in Engineering*, 46(2):177–204, 1999.
- 566 C. Giry, F. Dufour, and J. Mazars. Stress-based nonlocal damage model. *International Journal of Solids and Structures*, 48(25):3431 – 3443, 2011.
567 ISSN 0020-7683. doi: <https://doi.org/10.1016/j.ijsolstr.2011.08.012>.
- 568 M. A. Gutiérrez. Energy release control for numerical simulations of failure in quasi-brittle solids. *International Journal for Numerical Methods*
569 *in Biomedical Engineering*, 20(1):19–29, 2004.
- 570 M. A. Gutiérrez. Energy release control for numerical simulations of failure in quasi-brittle solids. *Communications in Numerical Methods in*
571 *Engineering*, 20(1):19–29, 2004. ISSN 1099-0887. doi: 10.1002/cnm.649.
- 572 J. Hadamard. *Leçons sur la propagation des ondes et les équations de l'hydrodynamique*. A. Hermann, 1903.
- 573 R. Hill. Acceleration waves in solids. *Journal of the Mechanics and Physics of Solids*, 10(1):1–16, 1962.
- 574 A. Hillerborg, M. Modeer, and P. Petersson. Analysis of crack formation and crack growth in concrete by means of fracture mechanics and finite
575 elements. *Cement and Concrete Research*, 6(6):773–781, 1976.
- 576 T. J. Hughes. *The finite element method: linear static and dynamic finite element analysis*. Dover Publications, 1987.
- 577 E. Lorentz and P. Badel. A new path-following constraint for strain-softening finite element simulations. *International journal for numerical*
578 *methods in engineering*, 60(2):499–526, 2004.
- 579 D. Magisano, L. Leonetti, and G. Garcea. Advantages of the mixed format in geometrically nonlinear analysis of beams and shells using solid
580 finite elements. *International Journal for Numerical Methods in Engineering*, 109(9):1237–1262, 2017.
- 581 D. Magisano, F. Liguori, L. Leonetti, D. de Gregorio, G. Zuccaro, and G. Garcea. A quasi-static nonlinear analysis for assessing the fire resistance
582 of reinforced concrete 3d frames exploiting time-dependent yield surfaces. *Computers & Structures*, 212:327–342, 2019.
- 583 J. Mandel. Conditions de stabilité et postulat de drucker. In *Rheology and Soil Mechanics/Rhéologie et Mécanique des Sols*, pages 58–68. Springer,
584 1966.
- 585 P. Massin, G. Ferté, A. Caron, and N. Moës. Pilotage du chargement en formulation x-fem: application aux lois cohésives. In *10e colloque national*
586 *en calcul des structures*, pages Clé–USB, 2011.
- 587 I. M. May and Y. Duan. A local arc-length procedure for strain softening. *Computers & structures*, 64(1):297–303, 1997.
- 588 S. May, J. Vignollet, and R. de Borst. A new arc-length control method based on the rates of the internal and the dissipated energy. *Engineering*
589 *Computations*, 2016.
- 590 J. Mazars. Application de la mécanique de l'endommagement au comportement non linéaire et à la rupture du béton de structure. *Thèse de docteur*
591 *es sciences, Université Pierre et Marie -PARIS 6*, 1984.
- 592 K. Moreau, N. Moës, N. Chevaugeon, and A. Salzman. Concurrent development of local and non-local damage with the thick level set approach:
593 Implementation aspects and application to quasi-brittle failure. *Computer Methods in Applied Mechanics and Engineering*, 327:306 – 326, 2017.
594 ISSN 0045-7825. doi: <https://doi.org/10.1016/j.cma.2017.08.045>. Advances in Computational Mechanics and Scientific Computation—the
595 Cutting Edge.
- 596 A. Needleman and J. Rice. Limits to ductility set by plastic flow localization. In *Mechanics of sheet metal forming*, pages 237–267. Springer, 1978.
- 597 J. Oliver, A. Huespe, and J. Cante. An implicit/explicit integration scheme to increase computability of non-linear material and contac-
598 t/friction problems. *Computer Methods in Applied Mechanics and Engineering*, 197(21):1865 – 1889, 2008. ISSN 0045-7825. doi:
599 <https://doi.org/10.1016/j.cma.2007.11.027>.
- 600 R. H. J. Peerlings, R. De Borst, W. A. M. Brekelmans, and M. G. D. Geers. Gradient-enhanced damage modelling of concrete fracture. *Mechanics*



- 601 of *Cohesive-frictional Materials*, 3(4):323–342, 1998.
- 602 P. Pegon and A. Anthoine. Numerical strategies for solving continuum damage problems with softening: application to the homogenization of
603 masonry. *Computers & structures*, 64(1-4):623–642, 1997.
- 604 T. Pohl, E. Ramm, and M. Bischoff. Adaptive path following schemes for problems with softening. *Finite Elements in Analysis and Design*, 86:12
605 – 22, 2014. ISSN 0168-874X. doi: <https://doi.org/10.1016/j.finel.2014.02.005>.
- 606 E. Ramm. Strategies for tracing the nonlinear response near limit points. In *Nonlinear finite element analysis in structural mechanics*, pages 63–89.
607 Springer, 1981.
- 608 G. Rastiello, C. Boulay, S. D. Pont, J. Tailhan, and P. Rossi. Real-time water permeability evolution of a localized crack in concrete under loading.
609 *Cement and Concrete Research*, 56:20 – 28, 2014. ISSN 0008-8846. doi: <https://doi.org/10.1016/j.cemconres.2013.09.010>.
- 610 G. Rastiello, J.-L. Tailhan, P. Rossi, and S. Dal Pont. Macroscopic probabilistic cracking approach for the numerical modelling of fluid leakage in
611 concrete. *Annals of Solid and Structural Mechanics*, 7(1):pp.1–16, Jan. 2015. doi: 10.1007/s12356-015-0038-6.
- 612 G. Rastiello, C. Giry, F. Gatuingt, and R. Desmorat. From diffuse damage to strain localization from an eikonal non-local (enl) continuum damage
613 model with evolving internal length. *Computer Methods in Applied Mechanics and Engineering*, 331:650 – 674, 2018. ISSN 0045-7825. doi:
614 <https://doi.org/10.1016/j.cma.2017.12.006>.
- 615 G. Rastiello, F. Riccardi, and B. Richard. Discontinuity-scale path-following methods for the embedded discontinuity finite element modeling of
616 failure in solids. *Computer Methods in Applied Mechanics and Engineering*, 349:431–457, 2019.
- 617 J. R. Rice. Localization of plastic deformation. Technical report, Brown Univ., Providence, RI (USA). Div. of Engineering, 1976.
- 618 B. Richard, G. Rastiello, C. Giry, F. Riccardi, R. Paredes, E. Zafati, S. Kakarla, and C. Lejouad. Castlab: an object-oriented finite element toolbox
619 within the matlab environment for educational and research purposes in computational solid mechanics. *Advances in Engineering Software*,
620 128:136 – 151, 2019. ISSN 0965-9978. doi: <https://doi.org/10.1016/j.advengsoft.2018.08.016>.
- 621 E. Riks. *The Application of Newton's Method to the Problem of Elastic Stability*. American Society of Mechanical Engineers, 1972.
- 622 E. Riks. An incremental approach to the solution of snapping and buckling problems. *International journal of solids and structures*, 15(7):529–551,
623 1979.
- 624 N. Singh, C. Verhoosel, R. de Borst, and E. van Brummelen. A fracture-controlled path-following technique for phase-field modeling of brittle
625 fracture. *Finite Elements in Analysis and Design*, 113:14 – 29, 2016. ISSN 0168-874X. doi: <https://doi.org/10.1016/j.finel.2015.12.005>.
- 626 A. Stanić and B. Brank. A path-following method for elasto-plastic solids and structures based on control of plastic dissipation and plastic work.
627 *Finite Elements in Analysis and Design*, 123:1 – 8, 2017. ISSN 0168-874X. doi: <https://doi.org/10.1016/j.finel.2016.09.005>.
- 628 F. Thierry, G. Rastiello, C. Giry, and F. Gatuingt. One-dimensional eikonal non-local (enl) damage models: Influence of the integration rule for
629 computing interaction distances and indirect loading control on damage localization. *Mechanics Research Communications*, 110:103620, 2020.
630 ISSN 0093-6413. doi: <https://doi.org/10.1016/j.mechrescom.2020.103620>.
- 631 T. Y. Thomas. *Plastic Flow and Fracture in Solids by Tracy Y Thomas*. Elsevier, 1961.
- 632 C. V. Verhoosel, J. J. Remmers, and M. A. Gutiérrez. A dissipation-based arc-length method for robust simulation of brittle and ductile failure.
633 *International Journal for Numerical Methods in Engineering*, 77(9):1290–1321, 2009a.
- 634 C. V. Verhoosel, J. J. C. Remmers, and M. A. Gutiérrez. A dissipation-based arc-length method for robust simulation of brittle and ductile failure.
635 *International Journal for Numerical Methods in Engineering*, 77(9):1290–1321, 2009b. ISSN 1097-0207. doi: 10.1002/nme.2447.
- 636 P. Verpeaux, A. Millard, T. Charras, and A. Combescure. A modern approach of large computer codes for structural analysis. *IASMiRT*, 1989.
- 637 Y. Wang and H. Waisman. An arc-length method for controlled cohesive crack propagation using high-order xfem and irwin's crack closure
638 integral. *Engineering Fracture Mechanics*, 199:235 – 256, 2018. ISSN 0013-7944. doi: <https://doi.org/10.1016/j.engfracmech.2018.05.018>.
- 639 O. C. Zienkiewicz, R. L. Taylor, and J. Z. Zhu. *The finite element method: its basis and fundamentals*. Elsevier, 2005.